The Thesis committee for Sarah Yvonne Greer
Certifies that this is the approved version of the following thesis:

A data matching algorithm and its applications in seismic data analysis

APPROVED BY

SUPERVISING COMMITTEE:

Dr. Sergey Fomel, Supervisor

Dr. Kyle Spikes

Dr. Clark Wilson

A data matching algorithm and its applications in seismic data analysis

by

Sarah Yvonne Greer

THESIS

Presented to the Faculty of

The University of Texas at Austin

in Partial Fulfillment

of the Requirements

for the Degree of

BACHELOR OF SCIENCE WITH HONORS

THE UNIVERSITY OF TEXAS AT AUSTIN

May 2018

Acknowledgments

I have received an incredible amount of support during my time as an undergraduate student. First and foremost, I'd like to thank my advisor, Dr. Sergey Fomel, for his helpful guidance over the past couple of years. I genuinely believe that working with him has beneficially shaped the trajectory of my life. Through his guidance and the opportunities he has given me, he has helped me to realize how much I truly enjoy learning, showed me the importance of reproducible computational research, introduced me to new ways of thinking about and approaching problems, and inspired me to continue my studies in graduate school. For all that, I will be forever grateful.

Many professors from the geological sciences and mathematics departments with whom I have interacted have also greatly helped me during my undergraduate career. I am especially thankful to Dr. Todd Arbogast, Dr. Jaime Barnes, Dr. Mark Cloos, Dr. Luc Lavier, Dr. Francesco Maggi, Dr. Richard Tsai, and my committee members, Dr. Kyle Spikes and Dr. Clark Wilson, for their guidance during my time at UT Austin.

I am also grateful to many students and research scientists I've had the pleasure of interacting with: Sean Bader, Luke Decker, Preston Fussee-Durham, Zhicheng Geng, Eric Goldfarb, Ben Gremillion, Tom Hess, Ken Ikeda, Harpreet Kaur, Dmitrii Merzlikin, Nam Pham, Mason Phillips, Kelly Regimbal, Karl Schleicher, Yunzhi Shi, Dr. Junzhe Sun, Dr. Yanadet Sripanich, Dr. Xinming Wu, Dr. Zhiguang Xue, and Dr. Yunan Yang.

I would especially like to thank the members of the Texas Consortium for

Computational Seismology (TCCS), of which I have been a part for the past two and a half years. Thank you all for your intellectually stimulating conversations, life advice, and for including me as "part of the group", despite the fact that I was only an undergraduate student. I will forever cherish the friendships and memories I have made with all of you during my time as a part of TCCS. You are an incredibly bright and enjoyable group, and I am fortunate to have had the opportunity to cross paths in life with every single one of you.

Last but not least, I would like to express my sincere gratitude to my family for all their love and support over the years. Esme, Joel, Sam, Atticus, and Kali—you all mean the world to me and I wouldn't be the person I am today without you in my life.

SARAH YVONNE GREER

The University of Texas at Austin
April 2018

A data matching algorithm and its applications in seismic data analysis

Sarah Yvonne Greer, B.S.

The University of Texas at Austin, 2018

Supervisor: Dr. Sergey Fomel

Data matching applications appear in many computational geophysics problems. In this thesis, I introduce a new efficient algorithm to aid in data matching that balances local frequency content between seismic data sets. Then, I provide a few examples where applying this algorithm to seismic data helps improve results. These applications include multi-component image registration, matching and merging high-resolution and legacy seismic images, and improving migration resolution by approximating the least-squares Hessian. The applications are illustrated by several 2D and 3D, real and synthetic data sets.

Table of Contents

List of Tables

List of Figures

Chapter 1

Introduction

Data matching is a conceptually simple problem that appears in many computational geophysics applications. Essentially, given two data sets, data matching can be thought of as finding the transformation from one data set to the other. This is useful in applications such as multi-component seismic image registration, where two separate seismic images, one P-wave image and one S- wave image, are acquired over the same area. These must be matched properly, as the two images are not temporally aligned and have different frequency and amplitude content, in order for them to be directly compared and interpreted.

Many other geophysics applications can be addressed from a data matching standpoint and fall under several main categories. One category is matching data of different physics, such as tying synthetic seismograms from well log data to surface seismic data (Herrera et al., 2014; Bader et al., 2018) and multicomponent seismic image registration (Fomel and Backus, 2003a; Fomel et al., 2005; Hardage et al., 2011), which is discussed in Chapter 3. Another category involves matching differently acquired data, such as time-lapse image registration (Fomel and Jin, 2009) and merging legacy and high-resolution seismic data (Greer and Fomel, 2018), which is a primary application in this thesis and is addressed in Chapter 4. The third category is matching data and ideal models, such as in deconvolution or approximating the inverse Hessian to improve migration resolution (Hu and Schuster, 1998; Guitton,

2017; Greer et al., 2018), which is discussed further in Chapter 5. The objective of these many data matching problems is to approximate the operation to match the data using a combination of three data matching operations—filtering, scaling, and shifting. In this thesis, I discuss these three data matching operators, outline several methods and applications of seismic data matching, and introduce a new method for matching frequency content between data sets.

The primary inspiration for much of the work in this thesis comes from the example of matching and merging high-resolution and legacy seismic images, as discussed by Greer and Fomel (2017b, 2018). In this example, two seismic data sets, each acquired over the same area but with different acquisition technologies, are first matched in frequency, amplitude, and time, before being merged together to produce a third image. This new image includes the best signal characteristics from the two initial images while minimizing their comparative weaknesses. Much of the theory behind Chapter 3 was developed in application to this example but was later extended to other examples. Therefore, I use the data from this application throughout much of this thesis.

DATA

This thesis refers to two primary data sets. The first pair, henceforth called the *Apache* data sets, are two 2D lines, acquired over the same area but with different methods, from the Gulf of Mexico. These two images are plotted in the *seismic* color map, as in Figure 3.1.

The second pair, the *P-cable* data sets, are two 3D volumes, acquired over the same area but with different methods, from a different area from the *Apache* data

sets, but also in the Gulf of Mexico (Petersen et al., 2010; Meckel et al., 2017). These two images will always be plotted in grayscale, as in Figure 3.5. In parts of this thesis, I show a 2D line from this 3D data set for simplicity of illustration.

Two other data sets, both 2D, were used in this thesis. In Chapter 3, I use two multi-component images to demonstrate an adaptation for the proposed frequency balancing algorithm in an application of multi-component image registration (Fomel, 2007a). In Chapter 5, I use the Sigsbee synthetic data set (Paffenholz et al., 2002) in the application of improving migration resolution using non-stationary matching.

OUTLINE

This thesis is organized as follows. In Chapter 2, I overview the theory behind the three data matching operations—scaling, shifting, and filtering. In Chapter 3, I introduce two methods for balancing local frequency content in seismic data sets. In Chapter 4, I show the first example of data matching: matching and merging high-resolution and legacy seismic images. In Chapter 5, I show an example of applying data matching to improve migration resolution. In Chapter 6, I provide concluding remarks. Finally, in the appendix, I include information on how to reproduce the results of this thesis.

Chapter 2

Background

Seismic data exhibit fundamentally non-stationary variations in attributes such as frequency and amplitude content. For example, Figure 2.1 shows a sample seismic image and its local frequency content (Greer and Fomel, 2017a). Data matching problems involve finding some transformation, or set of transformations, that can be applied to one data set to best match some attribute with another data set. In data matching applications, in particular, it is crucial to acknowledge the non-stationary variations present in seismic data. Therefore, any transformations we might apply in a data matching problem must be variant in all data dimensions to account for these non-stationary variations.

Local seismic attributes are useful in the analysis of these non-stationary variations (Fomel, 2007a). The calculation of these attributes uses iterative inversion with shaping regularization (Fomel, 2007b) to measure signal characteristics in local regions of data, rather than specifying windows or looking at instantaneous attributes. For the procedures described in this thesis, local attributes are more appropriate than instantaneous attributes. Take, for example, local frequency (Figure 2.1), as opposed to instantaneous frequency. Local frequency allows the comparison of frequency content in a local region of samples, as opposed to instantaneous frequency, which attempts to provide a point by point comparison of frequency values between images. Because the corresponding reflections between images might not be precisely

aligned in time, using the local frequency attribute to balance frequency content between images would allow for more accurate frequency balancing than instantaneous frequency. Additionally, local frequency is a more geologically accurate attribute than instantaneous frequency because it honors time-frequency uncertainty and does not contain physically unrealistic negative or unrealistic high frequency values (Fomel, 2007a).

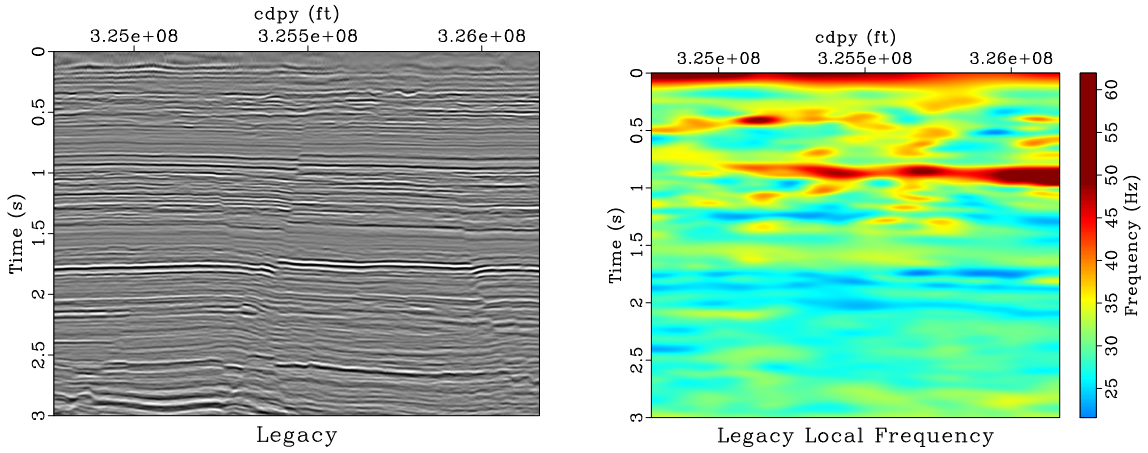

Figure 2.1: A seismic image (a) and its local frequency content (b). Because its local frequency varies both spatially and temporally, we can say its frequency content is smoothly *non-stationary*. chapter-background/../chapter-locfreq/merge legacy,low-freq

In this thesis, I propose solving data matching problems by balancing smoothly varying non-stationary attributes, such as local seismic attributes, between two data sets. This is done using three primary data matching operations—filtering, scaling, and shifting—to effectively balance these attributes across seismic data sets. These operations are applied to different data sets to match them correctly for analysis or further processing.

To demonstrate the three matching operations in action, I apply them consec-

utively to an example trace shown in Figure 2.2(a). The data used in this example comes from a line from the *P-cable* data sets. In this example, we want to find a transformation, or a set of transformations, to apply to the red trace to match with the black trace. I use the three data matching operators by first filtering (Figure 2.2(b)), then scaling (Figure 2.2(c)), and finally shifting (Figure 2.2(d)). These three operations are described in more detail in the following sections.

FILTERING

Perhaps one of the most visibly obvious differences between data sets comes from their difference in frequency content. For example, Figure 2.2(a) shows two traces that need to be matched; the red trace has visibly higher frequencies than the black trace which makes it difficult to observe that they may both contain data from the same model. This makes the correlation of these two signals, both visually and computationally, difficult as they have information in different frequency bands. In this situation, we want to remove the higher frequency variations from the red trace to match the lower frequency content of the black trace.

There are several ways to do this. A naïve first approach would be to apply a bandpass filter to the red trace such that the passband covers only frequencies that are present in the black trace. However, this stationary operation does not take into account the non-stationary frequency variations that may be naturally present in the data. In order to properly match the data in frequency content, we propose balancing local frequency content between data sets.

We can do this by applying a non-stationary triangle smoothing operator to the red trace to match the local frequency content of the black trace. We define the

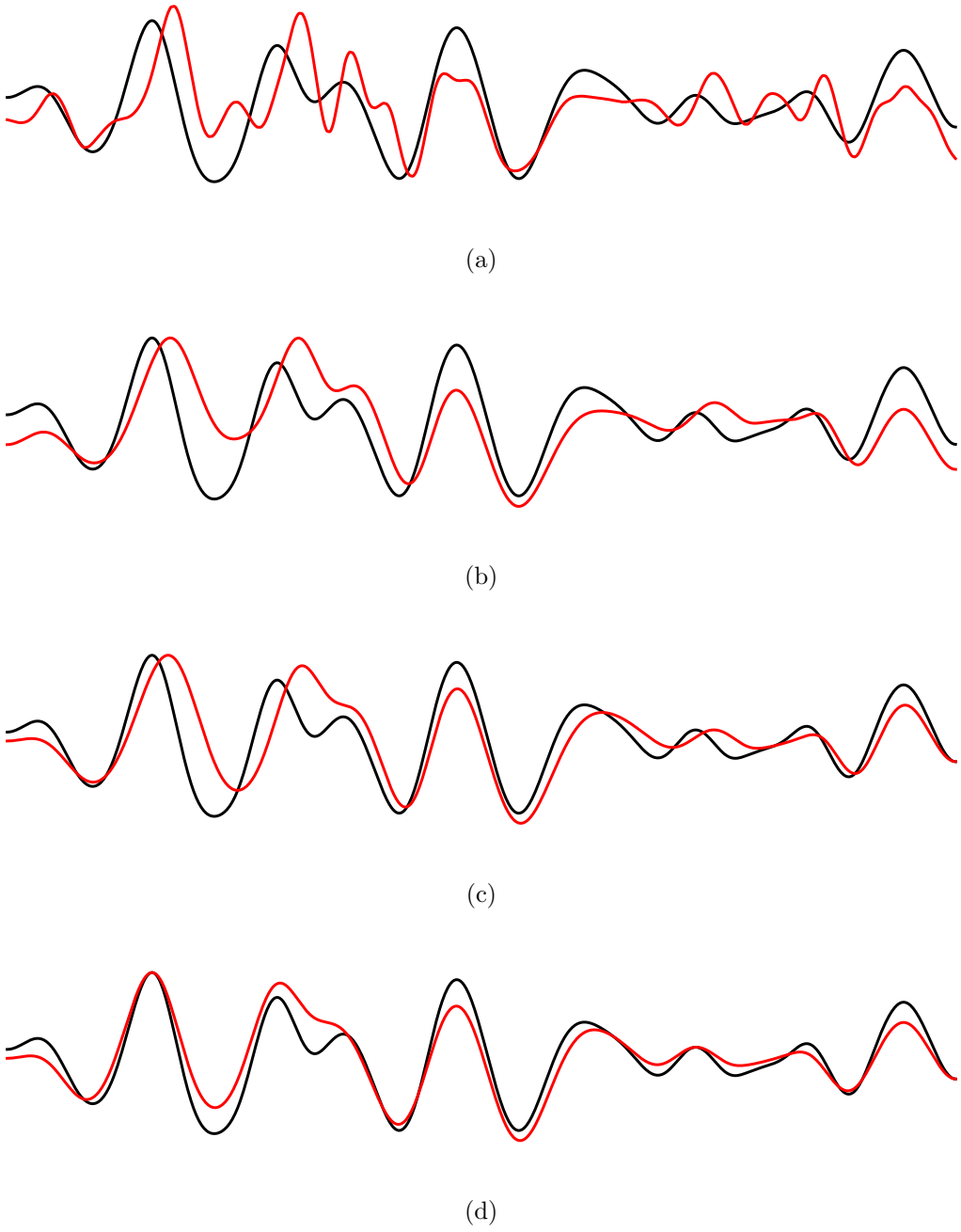

Figure 2.2: (a) Two traces that need to be matched—we will match the red trace to the black trace. (b) Red trace after filtering. (c) Red trace from (b) after scaling. (d) The final result: red trace from (c) after shifting, which now better matches with the black trace. The amount and order in which these operations is applied affects the final result (Figure 2.3). chapter-background/dmExample one0,one1,one2,one3

radius of this operator as the number of samples in a specified dimension that are averaged over in a triangle weight. We allow the radius to vary in all dimensions to account for the potential non-stationary frequency variations present in the data. This is a linear operation—if we represent the filtering operation by a matrix applied to the trace represented by a vector, the matrix would be diagonally banded, where the width of the band at a particular index is related to the size of the smoothing radius at that point.

Chapter 3 is dedicated to the discussion of how to find this frequency balancing operator. Figure 2.2(b) shows the two traces after balancing the local frequency content of the red trace to match the black trace.

SCALING

The second primary data matching operation is scaling. Amplitudes of the data we are trying to match may not be initially equivalent—scaling attempts to balance the amplitudes between these data. Scaling is also a linear operation and can be thought of as a diagonal operation; if the scaling operator is represented by a matrix multiplication to the data vector, this matrix only contains terms along the diagonal.

In this thesis, the diagonal scaling operator is found by first calculating the amplitude envelope of the data that need to be matched. Then, the scaling weight is calculated by smoothly dividing the amplitude envelopes of the two traces to find the diagonal elements of the scaling operator.

SHIFTING

If two events are misaligned in time, finding the transformation that correctly aligns these events is referred to as *shifting*. Dynamic time warping is a common algorithm used for the alignment of events of two time series, both for geophysical and other applications, as diverse as speech recognition and finance (Herrera and van der Baan, 2012; Hale, 2013; Müller, 2007; Tsinaslanidis et al., 2014).

In this thesis, I calculate the shifting operator by finding the time shifts that maximize local similarity between the two data sets. Local similarity extends the concept of local seismic attributes to global correlation coefficients and is effective for measuring the match of seismic events in a local region of samples (Fomel, 2007a).

In certain situations, these data must be correctly aligned in space instead of time; for example, in a depth-migrated image. In these cases, *time* shift is a misnomer. However, because the data we are typically dealing with are time series, the shifting operation that we find and apply is considered a function of time.

The result after finding and applying the time shift to the red trace to match it to the black trace is in Figure 2.2(d). This shifting operation is discussed in more detail in Chapters 3 and 4..

REPRESENTATION OF OPERATORS

Data matching problems are applicable for data sets that have the same physical model, yet have different characteristics that make their comparison difficult. For example, two seismic traces that were acquired over the same area but with different acquisition methods would benefit by applying data matching operations before their

direct comparison. These three operations can be applied to one data set to match it with the other.

When applying one operation, we assume the other two operators have already been applied, when this may not be the case. This is why we balance *local* seismic attributes instead of instantaneous ones—we want the match to be accurate in a region of data points rather than a point-by-point match. These operators must be smooth enough such that any misalignment of one attribute does not affect the result of balancing the others. For example, if a scaling operator is applied before the traces have been correctly aligned in time by shifting, too precise of an amplitude balancing operation could inadvertently balance amplitudes to incorrect events.

The order and amount of these operators affects the final result. After correcting for frequency variations, amplitude variations, and time shifts, additional corrections can be applied to further refine the match if necessary. These three operators are noncommutative, so the order in which they are applied matters. Applying filtering before scaling produces a different result from applying scaling before filtering. An illustration of this property is shown in Figure 2.3. In some cases, multiple rounds of applying these operators and in different orders may be beneficial for the best match.

Operator	**Representation**
Shifting	$\mathbf{d}_2(x) = \mathbf{d}_1(x + \mathbf{s}(x))$
Scaling	$\mathbf{d}_2(x) = \mathbf{w}(x)\mathbf{d}_1(x)$
Filtering	$\mathbf{D}_2(k) = \mathbf{W}(k)\mathbf{D}_1(k)$

Table 2.1: Mathematical representation of the three data matching operators.

A summary of the three data matching operations is shown in Table 2.1. In the stationary case, if scaling is weighting in the time domain, filtering is weighting

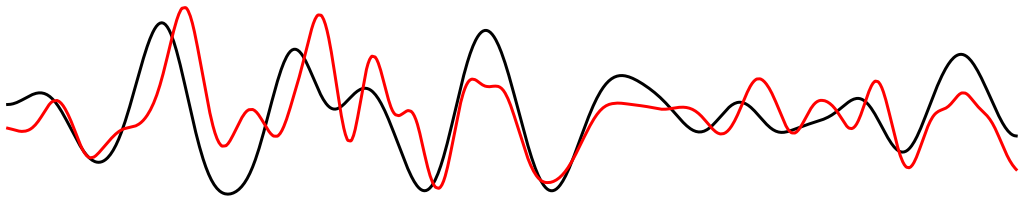

(a)

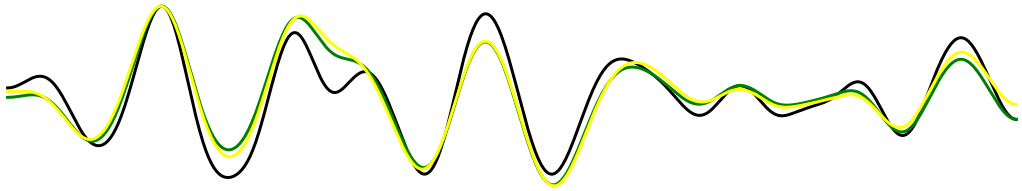

(b)

Figure 2.3: (a) A lower-resolution seismic trace (black) and a higher-resolution seismic trace (red) acquired over the same area. (b) Data matching operations are noncommutative—the order in which they are applied matters. When matching the red trace to the black trace, the green trace had first smoothing, then amplitude balancing, and finally shifting; the yellow trace had first amplitude balancing, then smoothing, and finally shifting. The operation order matters and affects the final result. chapter-background/dmExample bef,aft

in the Fourier domain. Chapter 3 discusses a few methods and examples of filtering, or frequency balancing, between two data sets.

Chapter 3

Balancing local frequency content in seismic data using non-stationary smoothing

Seismic data can experience non-stationary frequency variations caused by attenuation. This problem is encountered when matching multiple data sets, such as in multicomponent image registration, because signals with differing frequency content are hard to correlate. In this chapter, we introduce two methods for balancing frequency content between data sets while taking into account non-stationary frequency variations. Both methods involve finding and applying a non-stationary smoothing operator to minimize the local frequency difference between data sets. Numerical examples demonstrate that the proposed method improves multicomponent image registration and matching images of differing resolutions.

INTRODUCTION

Matching seismic data has many applications in geophysical processing methods, such as multi-component image registration, time-lapse image registration, matching well-ties to seismic data, and merging seismic data sets (Ursenbach et al., 2013; Fomel and Backus, 2003b; Lumley et al., 2003; Herrera and van der Baan, 2012). Typically, the workflow for matching data involves finding the optimal time shift, or amount

Parts of this chapter were first published in Greer and Fomel (2017a), Greer and Fomel (2017b), and Greer and Fomel (2018). This work was done under the supervision of Dr. Sergey Fomel.

of stretching and compressing, of one trace relative to the other that produces the greatest similarity between the two traces, as seen in dynamic time warping and local similarity scanning (Hale, 2013; Fomel and Jin, 2009; Herrera et al., 2014). However, when the two signals that need to be aligned have different spectral content, their comparison can be difficult. Seismic data contain non-stationary, or spatially and temporally variant, frequency content caused by attenuation. This problem was discussed in application to multicomponent image registration by Fomel and Backus (2003b), who applied frequency balancing methods to improve registration results. Liu and Fomel (2012) proposed using local time-frequency decomposition (LTFD) to balance frequencies between multicomponent data during registration. However, LTFD is a relatively computationally expensive method.

In this chapter, we propose methods for removing non-stationary frequency differences that limit the effectiveness of matching data. We suggest applying either of the proposed methods to processing flows that involve matching data before attempting to find the time shift to align their signal content. To balance frequency content, we use a non-stationary smoothing operator with an adjustable smoothing radius to apply to the higher frequency data set. Our first approach finds the smoothing operator directly, but it is based on the primary assumption that the data can be modeled by a summation of Ricker wavelets. Our second approach of finding the smoothing radius is based on understanding what the smoothing operator physically does, and takes the form of an optimization problem which is solved using an iterative method. We introduce these methods and apply them to examples of merging high-resolution and conventional seismic images and multicomponent image registration.

METHOD

Two signals of differing frequencies are more difficult to correlate than signals of similar frequencies. For example, Figure 3.5 shows two seismic images representing the same subsurface, except they have distinctly different spectral content, as shown in Figure 3.7(a). In order to be directly comparable, these two images should have similar frequency content. Here, we look at local frequency (Fomel, 2007a), which can be thought of as a smoothed estimate of instantaneous frequency (White, 1991). Local frequency is a more geologically accurate attribute than instantaneous frequency because it honors time-frequency uncertainty and does not contain physically unrealistic negative or extremely high frequency values (Fomel, 2007a).

In order to balance local frequency content, we propose smoothing the higher frequency data using a non-stationary triangle smoothing operator with an adjustable radius. Here, the radius at each point is the number of samples in time that that specific data point is averaged over in a triangle weight.

We find the temporally and spatially variable smoothing radius to apply to the higher frequency image to balance local frequency content with the lower frequency image by taking two approaches. The first approach is finding the smoothing radius based on assumptions of what the data we are looking at can be represented by, and the second approach is based on understanding physically what non-stationary smoothing does to a data set. Both approaches work well in different situations—the first approach is less computationally expensive than the second approach, but is only applicable when the two data sets fit the assumptions that are used to calculate what the smoothing radius is. The second approach finds the smoothing radius in an iterative manner, but it manages to work well for any data set given to it.

Theoretical smoothing radius

To demonstrate the effectiveness of finding the smoothing radius using this method, we use the *Apache* seismic data sets. The two initial images are shown in Figure 3.1, and their frequency content are shown in Figure 3.2(a).

To balance the non-stationary frequency variations between data sets, we use a simple triangle smoothing operator with an adjustable radius. Here, the radius at each point is the amount of time, in seconds, that that specific data point gets averaged over in a triangle weight in the temporal direction. We specifically look at local frequency (Fomel, 2007a), which is a time-dependent frequency attribute, and can be thought of as a smoothed estimate of instantaneous frequency (White, 1991).

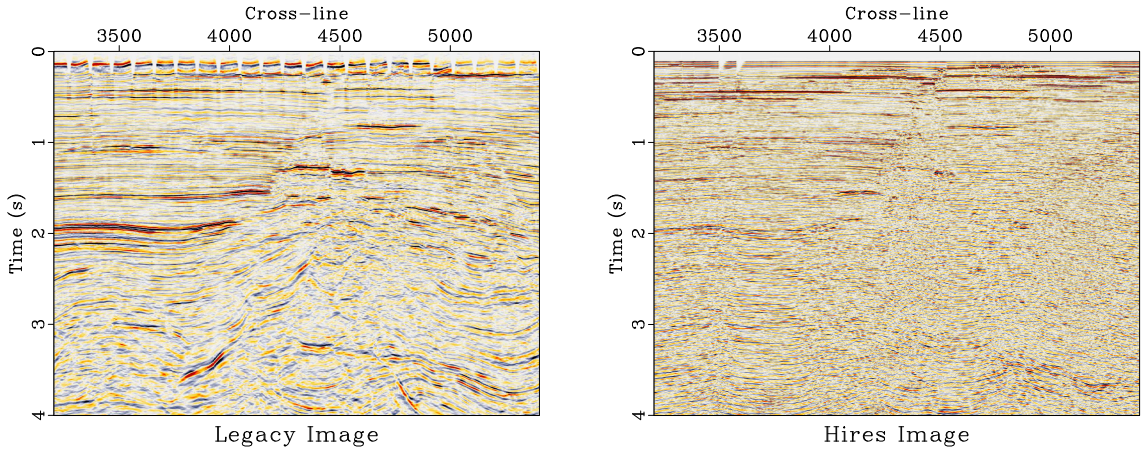

Figure 3.1: The initial legacy (a) and high-resolution (b) images. chapter-locfreq/../chapter-merge/apache legacy,hires

This method is based off of the primary assumption that the signal can be represented by Ricker wavelets convolved with the Earth's reflectivity series. Because the data we are working with are seismic amplitudes, this can be a good assumption (Gholamy and Kreinovich, 2014).

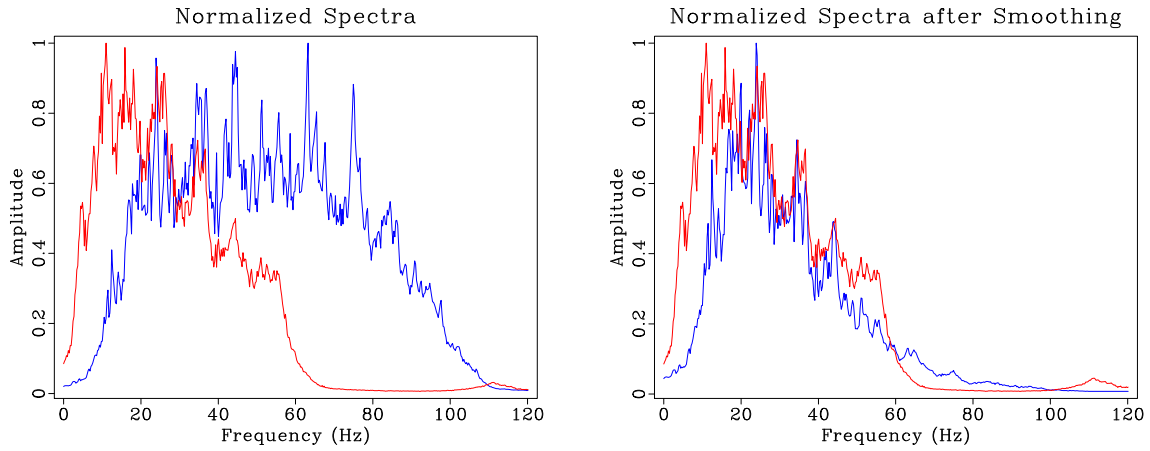

(a) (b)

Figure 3.2: Spectra for the entire image display of the legacy (red) and high-resolution (blue) images before (a) and after (b) spectral balancing using the theoretical method. chapter-locfreq/../chapter-merge/apache nspectra,hires-smooth-spec

The justification for triangle smoothing is that it is a simple approximation to Gaussian smoothing. The frequency response of the triangle smoothing filter (Claerbout, 1992) is

$$T(f) = \text{sinc}^2\left(\frac{2\pi f \Delta t}{2}\right) \approx 1 - \frac{(2\pi f)^2(\Delta t)^2}{12} \; . \tag{3.1}$$

This frequency response resembles that of a Gaussian:

$$G(f) = e^{-\alpha f^2} \approx 1 - \alpha f^2 \; . \tag{3.2}$$

If the signals' spectra can be represented by Ricker wavelets,

$$S_n(f) = A_n \left(\frac{f}{f_n}\right)^2 e^{-\left(\frac{f}{f_n}\right)^2} \tag{3.3}$$

where, in image n, S_n is the frequency spectrum, f_n is the peak frequency, and A_n is the amplitude, Gaussian smoothing can transform the signal to a different dominant frequency.

Because we are smoothing the high-resolution image to match it with the legacy image, we can relate the high-resolution frequencies, S_h, to the legacy frequencies, S_l, such that

$$S_l(f) = Ae^{-\alpha f^2} S_h(f) \tag{3.4}$$

where $A = A_l/A_h$,

$$\alpha = \frac{1}{f_l^2} - \frac{1}{f_h^2} , \tag{3.5}$$

and the subscripts l and h correspond to the legacy and high-resolution images, respectively.

Combining equations (3.1), (3.2), and (3.5) leads to the specification of the triangle smoothing radius as

$$\Delta t \approx \frac{1}{2\pi}\sqrt{12\left(\frac{1}{f_l^2} - \frac{1}{f_h^2}\right)} . \tag{3.6}$$

Here, Δt is the radius of smoothing, measured in seconds, applied to the high-resolution image to match the frequency content with the legacy image at each sample. The calculated smoothing radius for this data set is shown in Figure 3.3.

We measure local frequencies in both images and apply smoothing specified by equation (3.6) to the high-resolution image. Because this is only an approximation of what the smoothing radius should be under ideal conditions, we adjust the constant 12 in the equation to achieve a better match. In this example, this effectively reduces the difference between the spectral content of the images, as shown in Figure 3.2(b). Figure 3.4 shows the difference in local frequencies before and after smoothing. After smoothing, the frequency difference is minimized.

This method works well for simple data sets with overlapping frequency content. However, more complicated data sets, as seen in the next example, may require

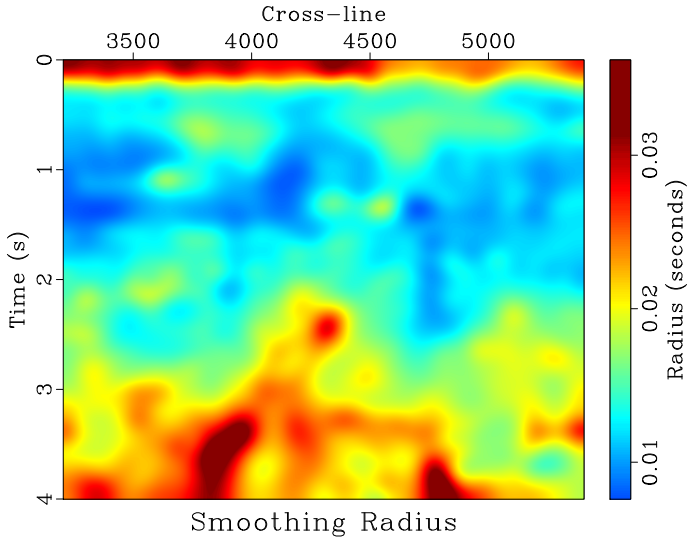

Figure 3.3: Calculated spatially and temporally variable smoothing radius. This represents the number of seconds in the temporal direction that the high-resolution image gets averaged over in a triangle weight to balance local frequency content with the legacy image at each sample. chapter-locfreq/../chapter-merge/apache rect

additional steps for successful frequency balancing.

Iterative method for calculating the smoothing radius

The theoretical smoothing radius works in some situations, like in the first example of Chapter 4, but it does not work in situations where little overlap is present in frequency content between data sets, like in the second example of Chapter 4. In this case, we use an iterative method to find what the smoothing radius should be that is based on the physical understanding of what smoothing is doing.

The goal of this method is to find the temporally and spatially variable smoothing radius, $\mathbf{R}$, that minimizes the difference in local frequencies between the two data

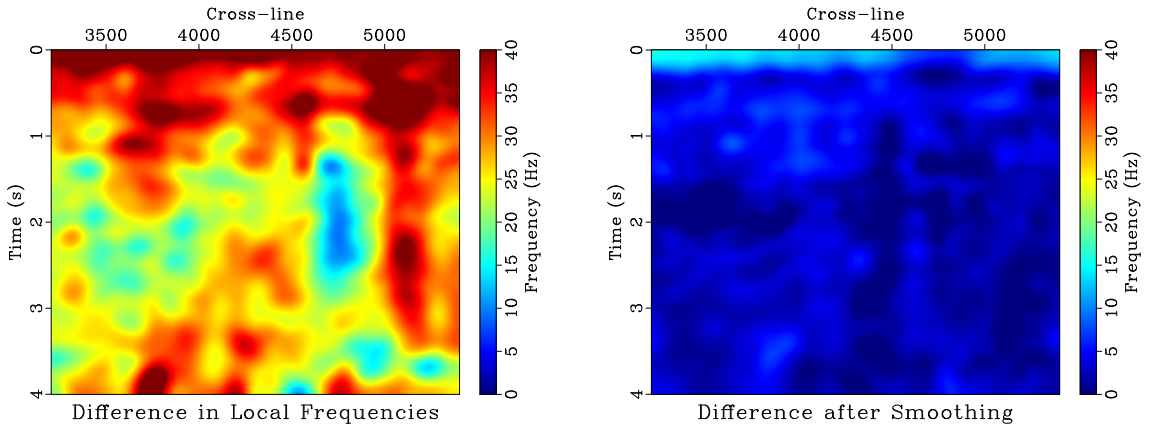

(a) (b)

Figure 3.4: Difference in local frequencies between the legacy and high-resolution images before (a) and after (b) balancing their frequency content by non-stationary smoothing. chapter-locfreq/../chapter-merge/apache freqdif,freqdif-filt

sets. This can be shown in the objective function

$$\min_{\mathbf{R}\in[1,N]} \left\| \mathbf{F}[\mathbf{S}_{\mathbf{R}}\mathbf{d}_h] - \mathbf{F}[\mathbf{d}_l] \right\| , \tag{3.7}$$

where $\mathbf{S}_{\mathbf{R}}$ is the non-stationary smoothing operator of smoothing radius $\mathbf{R}$, $\mathbf{d}_h$ is the higher frequency data, $\mathbf{d}_l$ is the lower frequency data, $\mathbf{F}$ is the local frequency operator, and N is the maximum size of the smoothing radius. Although smoothing is a linear operation, the smoothed data, $\mathbf{S}_{\mathbf{R}}\mathbf{d}_h$, depends non-linearly on $\mathbf{R}$. However, the objective from equation (3.7) is nearly convex, and we choose to use an intuitive iterative approach to find an approximate smoothing radius.

The main premise behind the method comes from the fact that, in general, the greater the smoothing radius, the more high frequencies are attenuated by smoothing.

1. The smoothing radius is too *small* at a specified point if, after smoothing, the higher frequency data has *higher* local frequency than the lower frequency data.

Thus, the smoothing radius must be *increased* at that point.

2. The smoothing radius is too *large* at a specified point if, after smoothing, the higher frequency data has *lower* local frequency than the lower frequency data. Thus, the smoothing radius must be *decreased* at that point.

We apply these assumptions using a line-search method:

$$\mathbf{R}^{(i+1)} = \mathbf{R}^{(i)} + c\mathbf{r}^{(i)}, \tag{3.8}$$

where $\mathbf{R}^{(i)}$ is the smoothing radius at the ith iteration, c is a scalar constant that can be thought of as the step length, and $\mathbf{r}^{(i)}$ is the residual at the ith iteration, which can be thought of as the search direction, and is defined as

$$\mathbf{r} = \mathbf{F}[\mathbf{S}_{\mathbf{R}}\mathbf{d}_h] - \mathbf{F}[\mathbf{d}_l]\ . \tag{3.9}$$

It can be noted that when equation (3.9) is positive, the higher frequency data still has a higher local frequency value at that specific point than the lower frequency data, thus the higher frequency data is under-smoothed and the smoothing radius should be increased at that point. This follows the form of the first assumption. The second assumption is used when equation (3.9) is negative. When equation (3.9) is zero, the correct radius has been found and no further corrections are made. Thus, it is justifiable to set the search direction from equation (3.8) equal to the residual.

Using the assumptions, we can choose an initial guess for the smoothing radius and continually adjust the smoothing radius until we achieve the desired result of balancing the local frequency content between the two data sets. In practice, this method produces an acceptable solution in approximately 5 iterations and exhibits sublinear convergence. After smoothing the higher frequency data with the estimated

radius, we use the lower frequency and smoothed higher frequency data to estimate time shifts and align the two data sets.

This method is applicable to workflows that require matching data with different frequency content. Here, we demonstrate that using this algorithm to match high-resolution and legacy seismic images improves the results.

High-resolution seismic data, such as those acquired with the P-cable acquisition system, can produce very detailed images of the near subsurface (Meckel and Mulcahy, 2016). When compared to conventional seismic images, high-resolution images have a higher dominant frequency and a wider frequency bandwidth. However, they usually lack low frequency content and depth coverage that is present in conventional seismic images. As a result, successful interpretation of high-resolution images can be aided by matching with legacy data coverage over the same area.

Example legacy and high-resolution images of the same subsurface are shown in Figure 3.5. The first step in matching the two images is to ensure that they both have a similar frequency bandwidth so they are directly comparable. The average frequency spectra for the two images are shown in Figure 3.7(a). From this, it is evident that there is almost no overlap in frequency bandwidth between the two images. To address this problem, we apply a low-cut filter to the legacy image to remove some of the lower frequencies that are simply not present in the high-resolution image. Next, we implement the method described in the previous section to balance local frequency content between the two images. The difference in local frequencies (residual, by equation 3.9) between the high-resolution and legacy images before balancing frequency content and after 5 iterations of the algorithm in equation (3.8) is shown in Figure 3.8. After balancing local frequencies, the images show a similar

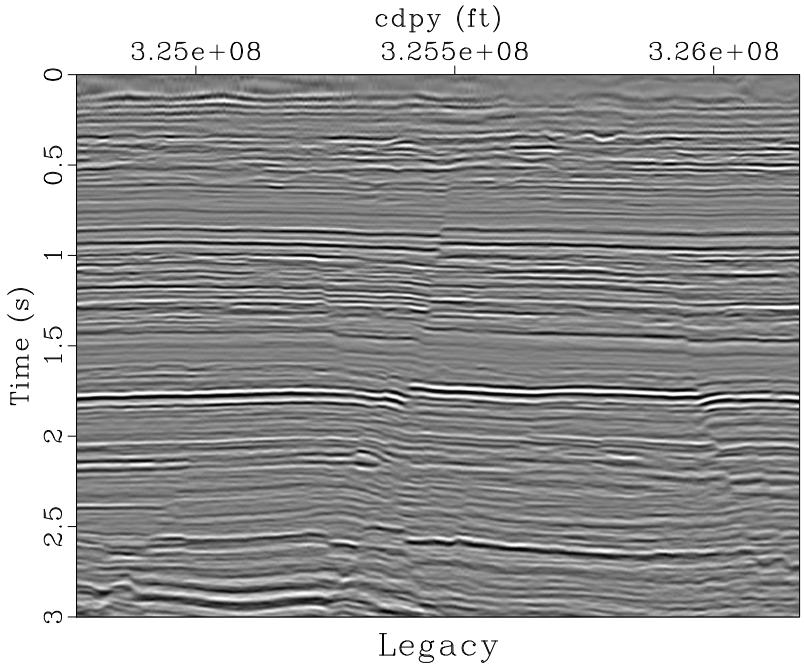

(a)

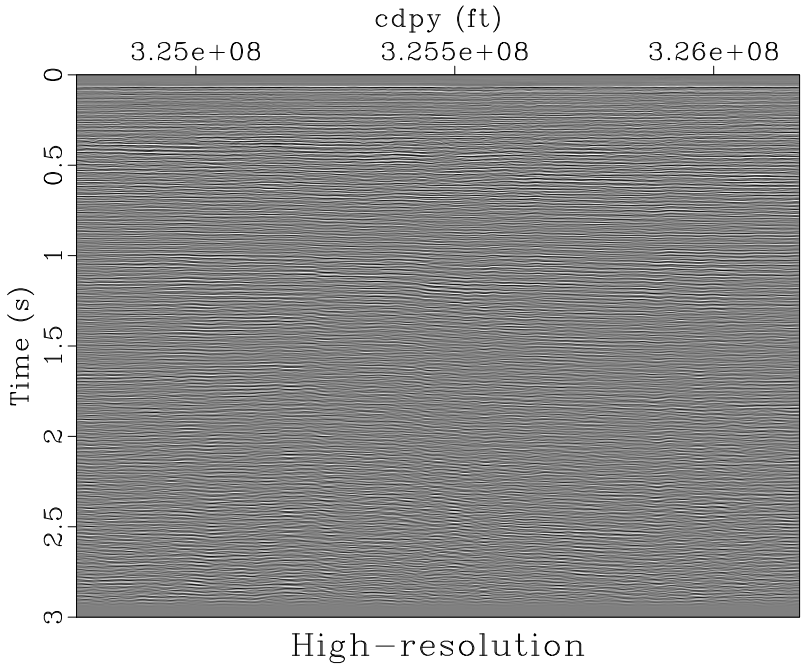

(b)

Figure 3.5: Initial legacy (a) and high-resolution (b) images. These images show the same subsurface geology, but look remarkably different as the high-resolution image has distinctly higher frequency content than the legacy image. chapter-locfreq/merge legacy,hires-agc

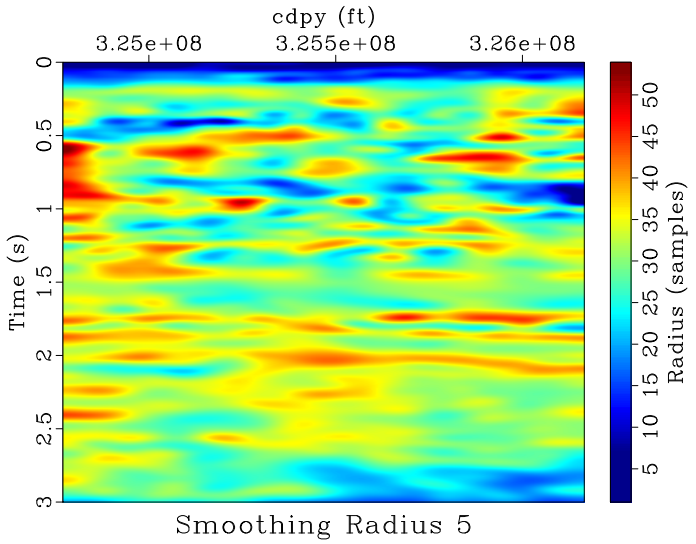

Figure 3.6: The smoothing radius, which is a function of time and space, this method produces after 5 iterations. This represents the number of samples in time that the high-resolution image needs to be smoothed over in a triangle weight to balance local frequency content with the legacy image. chapter-locfreq/merge rect5

spectral bandwidth (Figure 3.7(b)), which helps increase the correlation between the two images and makes matching reflections better defined.

After the frequency content is matched, the optimal time shift is found to align signal content between the legacy and high-resolution images. We then apply this time shift to the original high-resolution image—the frequency content is only degraded for the purpose of finding the time shift.

An application of aligning the high-resolution and legacy images is discussed in Chapter 4.

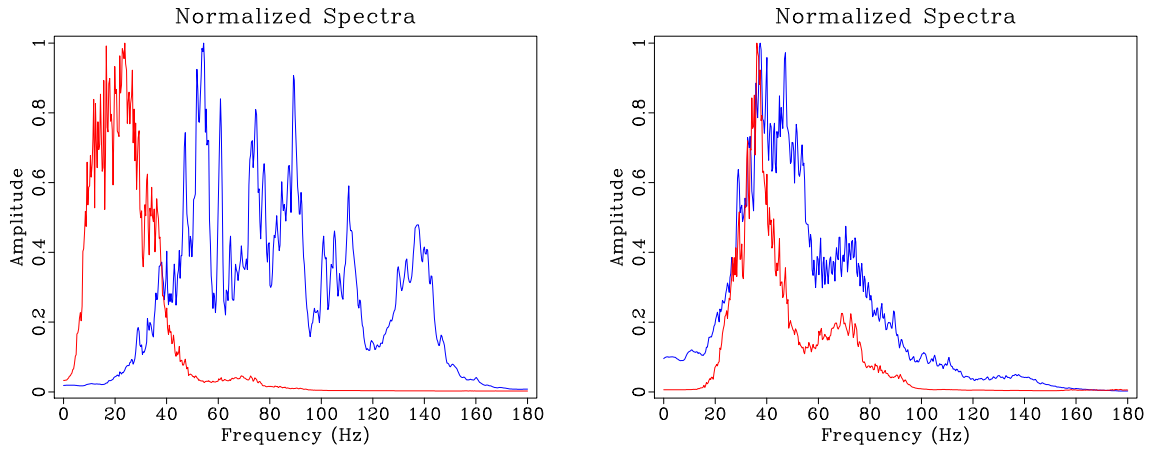

(a) (b)

Figure 3.7: Spectral content of the legacy (red) and high-resolution (blue) images before (a) and after (b) spectral balancing using the theoretical method. chapter-locfreq/merge nspectra-orig,high-smooth-spec5

Iterative method for calculating the smoothing radius: A modification

The algorithm previously presented works well in cases when one data set has clearly higher frequency content than the other. However, in some cases, the two data sets may have similar local frequency content, but they might still need to be matched. We illustrate a modified version of the previous algorithm by demonstrating it on an example of multi-component seismic image registration.

Multicomponent seismic image registration is an important step before the interpretation of P and S images of the subsurface. It involves warping the space of S images to align reflections with the analogous reflections of P images (Fomel and Backus, 2003b; Fomel et al., 2005).

Figure 3.9 shows PP and SS images from a 9-component seismic survey (Fomel, 2007a). To properly register the images, we follow the method proposed in Fomel

et al. (2005). It consists of three primary steps: (1) initial registration of PP and SS images using initial interpretation and well-log analysis; (2) balancing frequency and amplitude content; and (3) final registration using residual local similarity scanning. We incorporate our method of balancing frequency content into the second step in this process.

Before initial registration, the PP image has much higher frequency content than the SS image. After the SS image is temporally compressed to PP time for initial registration, the two images have more similar frequency content. However, additional frequency balancing is still needed before residual registration. This poses a problem as neither image has distinctly higher frequencies than the other, so both images need to be smoothed in different areas to balance frequency content. In order to do this, we modify the proposed method to include two separate smoothing operators—one for each image.

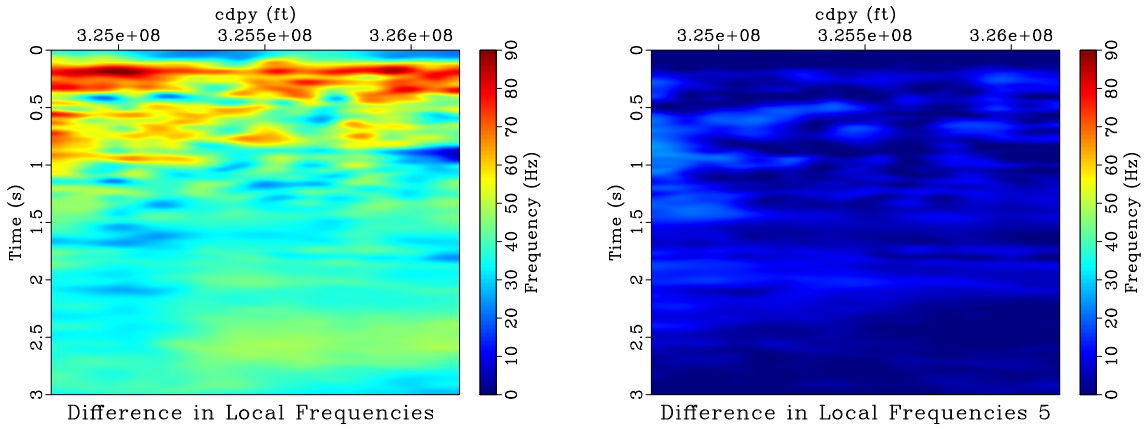

(a) (b)

Figure 3.8: Difference in local frequencies (residual) between the legacy and high-resolution images before (a) and after (b) the 5th iteration of frequency balancing. chapter-locfreq/merge freqdif,freqdif-filt5

We modify the objective in equation (3.7) as

$$\min_{\mathbf{R}\in[-N,-1]\cup[1,N]} \left\| \mathbf{F}[\mathbf{S}_{\mathbf{R}_p}\mathbf{d}_p] - \mathbf{F}[\mathbf{S}_{\mathbf{R}_s}\mathbf{d}_s] \right\| , \tag{3.10}$$

where $\mathbf{d}_p$ and $\mathbf{d}_s$ are the PP and SS images, respectively, and $\mathbf{S}_{\mathbf{R}_p}$ and $\mathbf{S}_{\mathbf{R}_s}$ are the non-stationary smoothing operators for the PP and SS images, respectively. We also modify the residual from equation (3.9) as

$$\mathbf{r} = \mathbf{F}[\mathbf{S}_{\mathbf{R}_p}\mathbf{d}_p] - \mathbf{F}[\mathbf{S}_{\mathbf{R}_s}\mathbf{d}_s] \, . \tag{3.11}$$

The ideal radius is still found using the same line-search from equation (3.8), except we allow the smoothing radius to be negative. Physically, a negative smoothing radius would signify that the image should be sharpened at that particular point instead of smoothed. In this case, instead of trying to sharpen the PP image at that particular point, we choose to smooth the SS image by the negative part of the smoothing radius. Thus, we define the ith components of $\mathbf{R}_p$ and $\mathbf{R}_s$ as

$$R_{p,i} = \begin{cases} R_i & \text{if } R_i \geq 1 \\ 1 & \text{otherwise} \end{cases} \tag{3.12}$$

and

$$R_{s,i} = \begin{cases} |R_i| & \text{if } R_i \leq -1 \\ 1 & \text{otherwise} \end{cases} \tag{3.13}$$

where R_i is the ith component of $\mathbf{R}$ and a radius of 1 represents no smoothing. This allows each image to be smoothed in different areas to balance the frequency content between the two images.

The results of using this spectral balancing method are shown in Figure 3.10. Comparable results were achieved in Liu and Fomel (2012), who used local time-frequency decomposition (LTFD) to balance the spectral content between the two

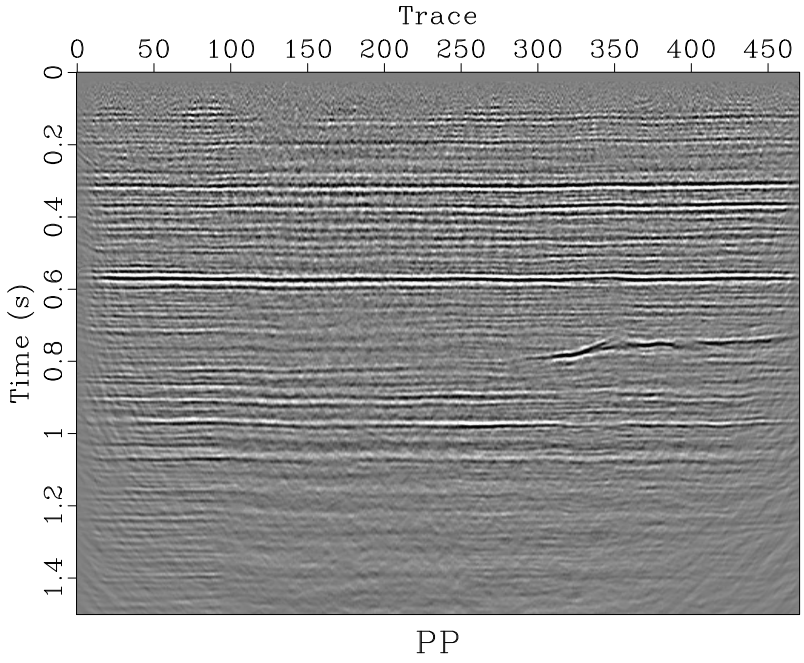

(a)

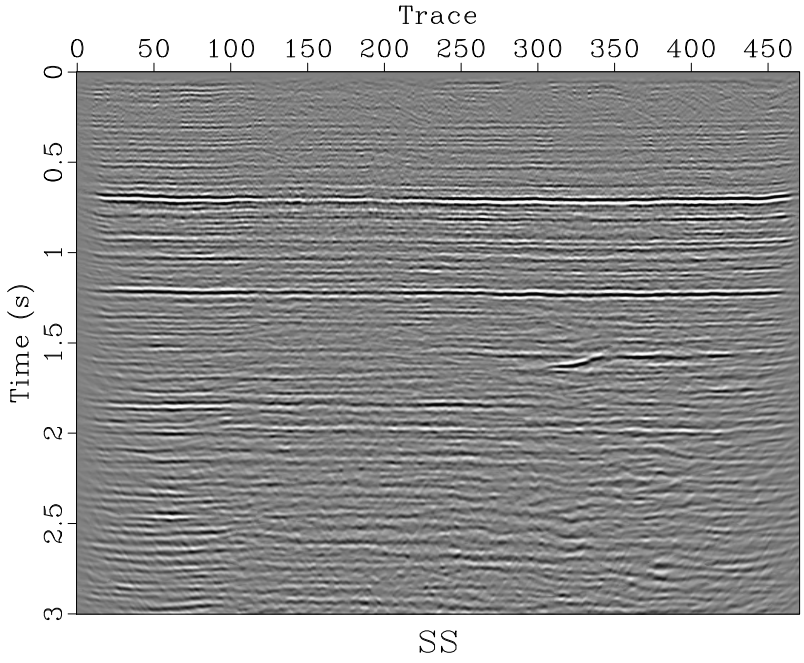

(b)

Figure 3.9: Initial PP (a) and SS (b) images. chapter-locfreq/vecta pp,ss

images. However, the method we propose in this chapter is more straightforward and significantly less computationally expensive.

So far, this algorithm and its modification have been discussed when the smoothing radius is only calculated along one dimension. However, Chapter 5 provides an application where the smoothing radius is calculated in multiple directions.

CONVERGENCE ANALYSIS

Because this algorithm was developed from observations and intuition based on what smoothing is physically doing, no error analysis or convergence criteria has been developed in this thesis. However, it is observed that this algorithm generally exhibits sublinear convergence. Additionally, the initial guess for what the smoothing radius should be negligibly impacts the final result. Figure 3.11(a) shows the convergence of the algorithm from equation (3.8) when applied to the *P-cable* data set from the second example in this chapter (Figure 3.5). It is evident that no matter the initial guess, the resulting convergence is relatively unaffected, and with the correct choice of step length c, converges in few iterations. After convergence, continuing iterations do not affect the final result.

Figure 3.11(b) shows the convergence when choosing different values of c, the step length from Equation (3.8). From this, it is evident that the step length is important for fast and stable convergence. If too large a step length is chosen, the method does not converge to the ideal solution. If the step length is too small, the algorithm takes many more iterations to converge. With the "correct" step length, however, the algorithm usually converges in fewer than 10 iterations in practice.

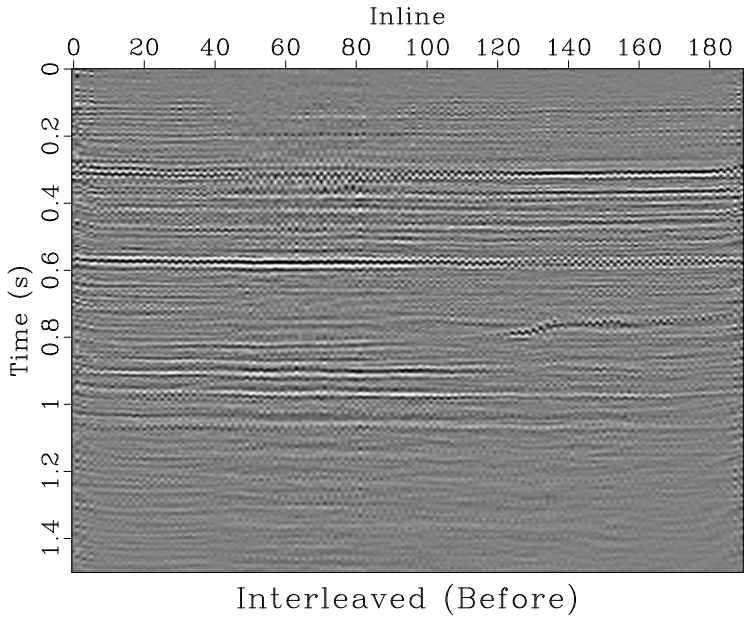

(a)

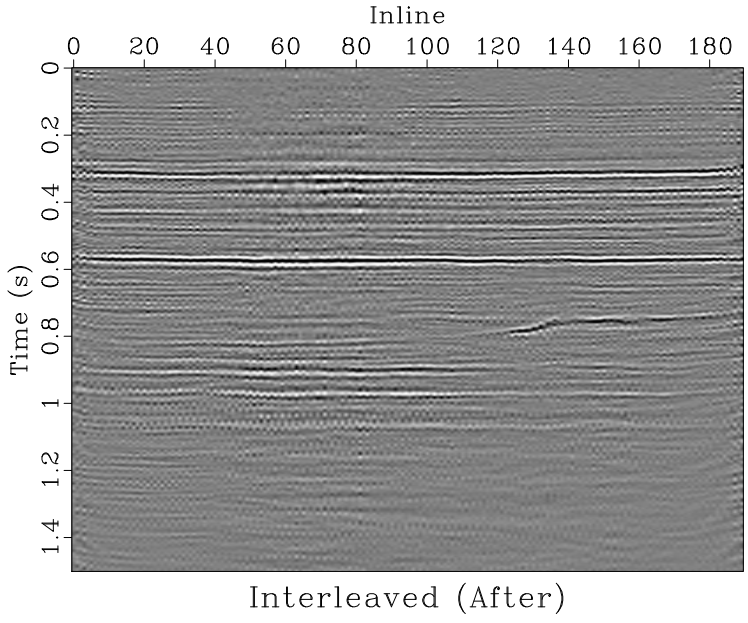

(b)

Figure 3.10: Interleaved PP and warped SS traces before (a) and after (b) frequency balancing and residual registration. After registration, the signal content between the two initial images is more aligned; for example, the reflections around 0.3 and 0.6 s. This indicates a successful registration. chapter-locfreq/vecta before,after

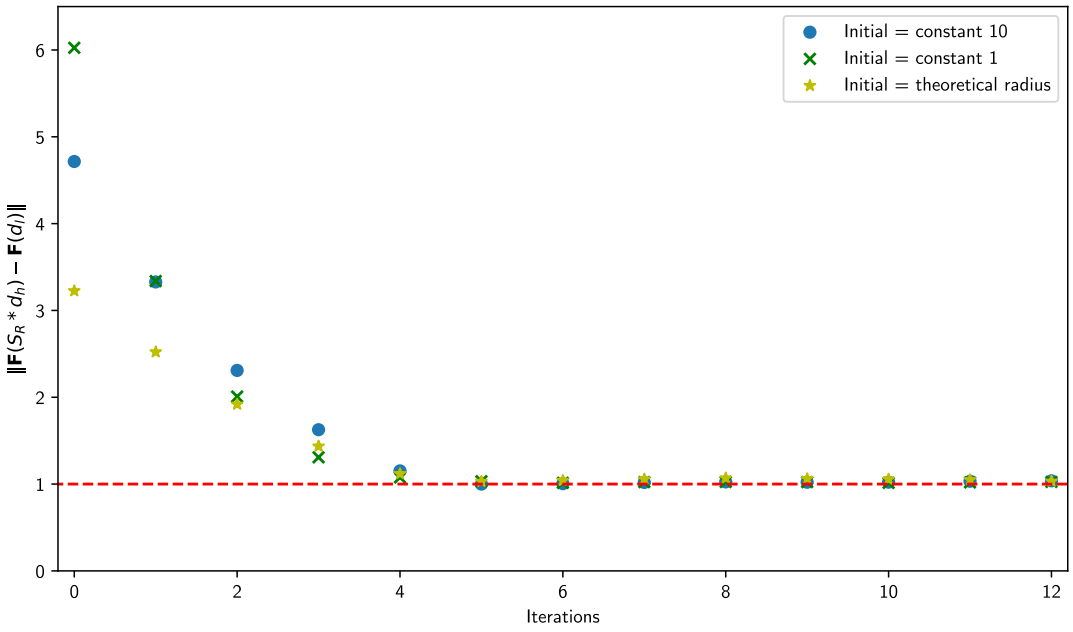

(a)

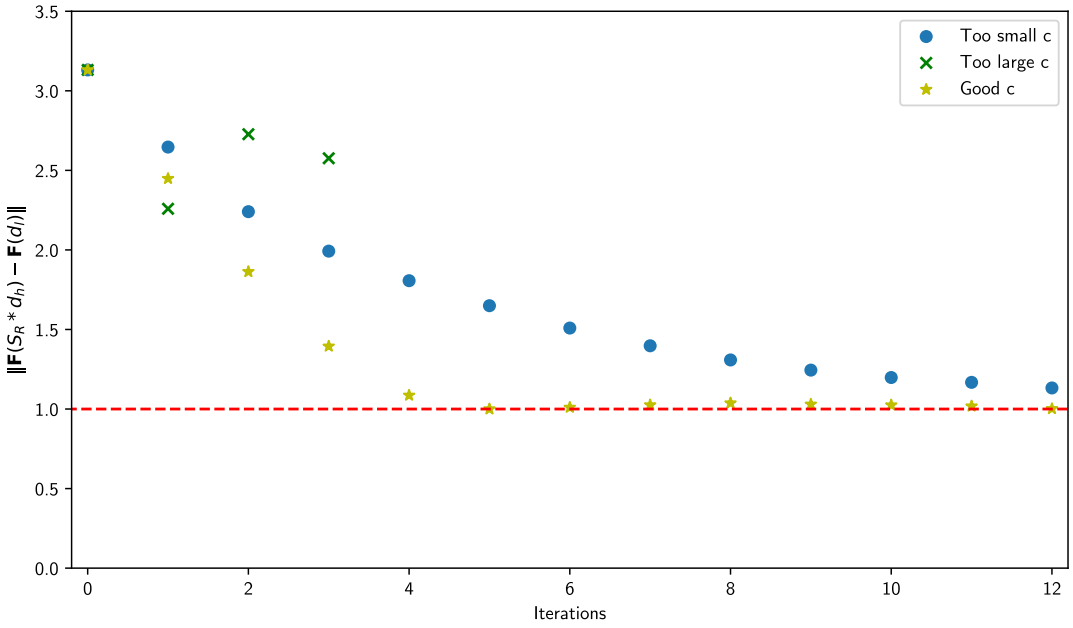

(b)

Figure 3.11: Convergence of the algorithm from Equation (3.8) for (a) different initial guesses, and (b) different choices of c, the step length, using the theoretical radius as the initial guess. chapter-locfreq/convergence all,scalar

CONCLUSIONS

Comparing signals with differing frequency content is difficult because signals with differing frequencies are hard to correlate. In this chapter, we proposed two methods of balancing frequency content between data. The first one takes a theoretical approach of what we expect the data to be, and the second one takes the form of an optimization problem solved by a simple iterative algorithm. This algorithm is a relatively inexpensive and effective method compared to previously proposed methods of balancing frequencies between data sets. We applied these methods to examples of matching seismic images of differing resolution and for multicomponent image registration.

ACKNOWLEDGMENTS

We thank the sponsors of the Texas Consortium for Computational Seismology (TCCS) for their financial support.

Chapter 4

Matching and merging high-resolution and legacy seismic images

When multiple seismic surveys are acquired over the same area using different technologies that produce data with different frequency content, it may be beneficial to combine these data to produce a broader bandwidth volume. We have developed a workflow for matching and blending seismic images obtained from shallow high-resolution seismic surveys and conventional surveys conducted over the same area. The workflow consists of three distinct steps: (1) balancing the amplitudes and frequency content of the two images by non-stationary smoothing of the high-resolution image, (2) estimating and removing variable time shifts between the two images, and (3) blending the two images together by least-squares inversion. Our workflow is applied successfully to images from the Gulf of Mexico.

INTRODUCTION

Modern high-resolution seismic acquisition systems, such as P-cable (Petersen et al., 2010; Meckel and Mulcahy, 2016), can produce detailed images of the subsurface at shallow depths. These images often need to be compared with those previously produced using legacy images from conventional seismic acquisition. In comparison with

Parts of this chapter were first published in Greer and Fomel (2017b). The peer-reviewed journal version appears as Greer and Fomel (2018). This work was done under the supervision of Dr. Sergey Fomel.

high-resolution images, conventional images have generally lower frequency content and correspondingly lower resolution, but better signal content at greater depth. To reconcile the differences between the two types of images, they need to be properly matched.

Analogous problems occur when interpreting images from multicomponent seismic acquisition. In particular, single-component PP and converted PS images often exhibit significantly different frequency content and need to be balanced for accurate registration (Hardage et al., 2011; Fomel and Backus, 2003a; Fomel et al., 2005).

When multiple data sets are acquired over the same area using different technologies, it is likely that these data sets contain signal content from different frequency bands, which correspondingly contain unique information about the subsurface. In order to utilize all available information, it may be beneficial to produce a consolidated broad-bandwidth volume that combines these data sets. Many previous methods of seismic data merging have been developed for the purpose of increasing the spatial coverage of the merged volume by combining data from partially overlapping areas. This usually involves steps such as rebinning for data alignment, along with spectral and phase matching. As a result, both the initial and resultant merged images poses similar signal characteristics, most notably spectral content (Mohan et al., 2007; Zhou et al., 2014; Al-Inaizi et al., 2004). However, previously Carter and Pambayuning (2009) were successful in applying a frequency domain merge to two separate seismic volumes over the same area to broaden the effective bandwidth.

In this chapter, we consider the problem of matching seismic images obtained in the same area with different resolution. Using techniques borrowed from multi-

component image processing (Fomel et al., 2005), we propose a multistep approach. First, we balance the two images in amplitude and frequency content. As a result, the resolution of the high-resolution image is temporarily degraded to match the resolution of the legacy data. Next, we measure shifts between images using local similarity scanning (Fomel, 2007a; Fomel and Jin, 2009). Finally, when the images are aligned and matched, we create a blended image using least-squares inversion in the time domain. The blended image has a wider frequency bandwidth than the two initial images, along with coherent signal content with depth from the legacy image and detailed shallow coverage from the high-resolution image.

We test the proposed approach using data from the Gulf of Mexico. A 2D image is used to illustrate the method, followed by an example applied to 3D data.

METHOD

The initial legacy and high-resolution example images are shown in Figure 4.1. They both underwent standard marine processing flows and are assumed to be optimally processed. The images show similar structures, particularly at shallow depths, but with strikingly different resolution. The main difference comes from the broader frequency bandwidth of the high-resolution image in comparison with that of the legacy image. Therefore, our first step in comparing the two images is balancing their spectral content.

Balancing spectral content

Analyzing the spectra of the legacy and high-resolution images, as seen in Figure 3.2(a), it is clear that the high-resolution image has a wider range of frequencies

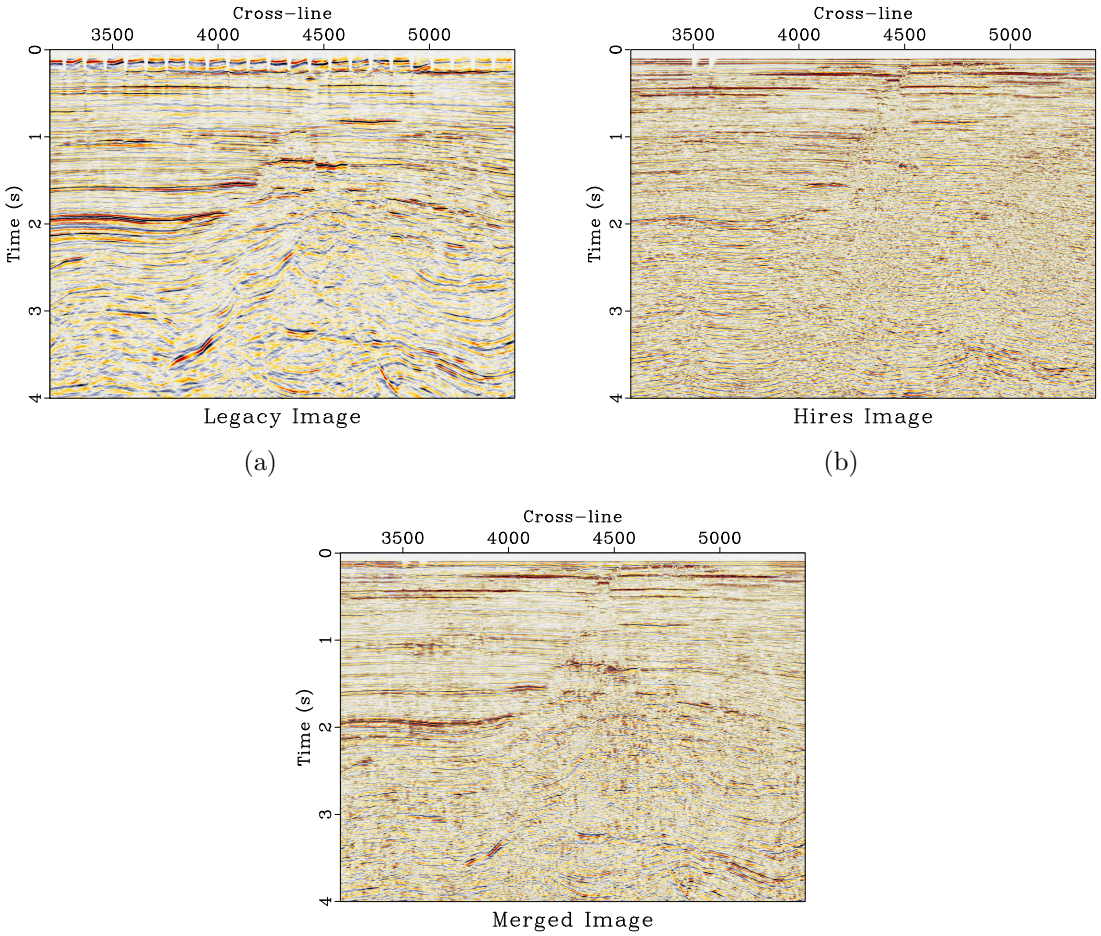

Figure 4.1: The initial legacy (a) and high-resolution (b) images. The merged image (c) is the final product of the proposed workflow: the combination of both the legacy and high-resolution images. chapter-merge/apache legacy,hires,merge2-reverse

with a higher dominant frequency than the legacy image. In order to match these images, our first step is to balance their spectral content. We can achieve this by attenuating the high frequencies of the high-resolution image to match the lower frequency content of the legacy image. One approach to frequency balancing is to apply a stationary bandpass filter to the high-resolution image. However, this does not take into account local frequency variations in each image caused by seismic wave attenuation. A more effective method, which accounts for temporally and spatially variable frequency content that is present in most seismic data, is to apply a non-stationary filter using frequency information from both images. To accomplish this, we use a simple triangle smoothing operator with an adjustable radius. Here, the radius at each point is the amount of time, in seconds, that that specific data point gets averaged over in a triangle weight in the temporal direction. In this example, we find the radius of smoothing using the theoretical approach described in Chapter 3, so

$$\Delta t \approx \frac{1}{2\pi}\sqrt{12\left(\frac{1}{f_l^2}-\frac{1}{f_h^2}\right)}\,. \tag{4.1}$$

Here, f_l and f_h are the local frequencies of the legacy and high-resolution images, respectively, and Δt is the radius of smoothing, measured in seconds, applied to the high-resolution image to match the frequency content with the legacy image at each sample. The spectral content of the high resolution image after balancing local frequencies clearly closer resembles that of the legacy image, as shown in Figure 3.2(b).

This method works well for simple data sets with overlapping frequency content. However, more complicated data sets, as seen in the next example, may require additional steps for successful frequency balancing.

In addition to frequency balancing, we initially attempted to account for wavelet phase differences between data sets at this step. However, we saw this had a negligible impact on the final result, so we decided not to include it in this method.

Measuring time shifts

After balancing the spectral content, we attempt to account for possible time shifts of the high-resolution image relative to the legacy image, which can be caused by changes in acquisition and processing parameters. We measure this shift using local similarity scanning (Fomel, 2007a; Fomel and Jin, 2009). In this method, we detect the relative time shift by first calculating the local similarity at different time shifts of the high-resolution image relative to the legacy image (Fomel and Jin, 2009). From this, the trend of the highest similarity is picked and represents the relative time shift between the two images.

Next, we apply the estimated time shift to the original high-resolution image—the frequency content is only degraded for the purpose of finding the time shift that best aligns the signal content between the two images. The differences between the two images before and after the time shift correction are shown in Figure 4.2, and demonstrate a noticeably better match resulting from the time shift. Similar results were achieved using amplitude-adjusted plane-wave destruction, which involves balancing amplitudes and temporally aligning the data sets simultaneously (Phillips and Fomel, 2016).

Creating the blended image

Because the high-resolution and legacy images contain information about the same subsurface, we can attempt to create an optimal image of this area by blending

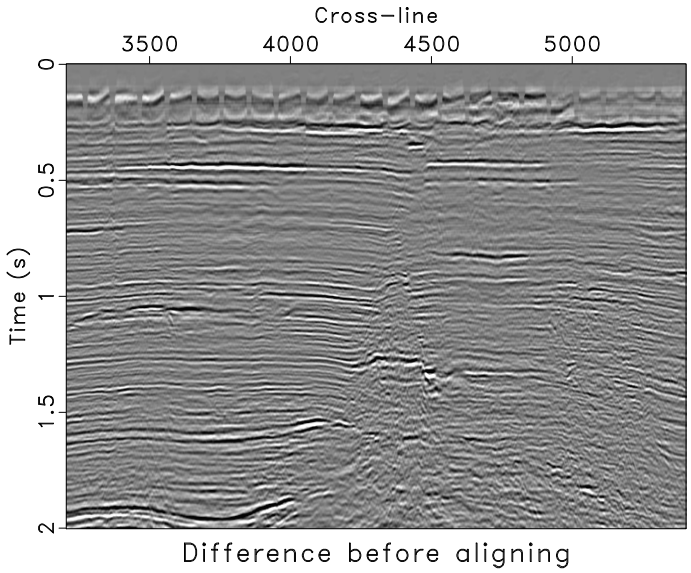

(a)

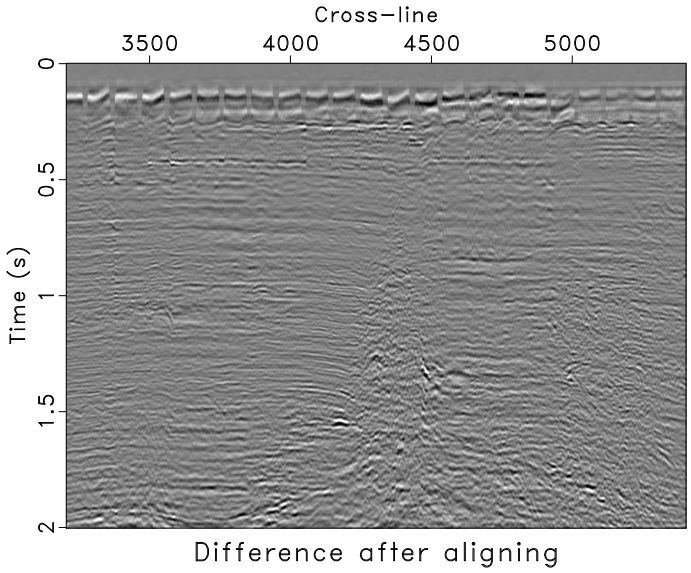

(b)

Figure 4.2: Difference between the legacy and smoothed high-resolution images before (a) and after (b) aligning the data sets. Before accounting for time shifts, much of the signal content did not align in time, so coherent reflections were subtracted out. After accounting for time shifts, the reflections are more aligned, so much of the subtracted information is noise. chapter-merge/apache diff0,diff1

the two images together to combine the strengths of each while minimizing their weaknesses. We can achieve this by imposing two conditions. First, the blended image should match the high-resolution image, particularly in the shallow part. Second, after smoothing with the non-stationary smoothing operator, the blended image should match the legacy image. We combine the two conditions together in the least-squares system

$$\begin{bmatrix} \mathbf{W_h} \\ \mathbf{W_l S} \end{bmatrix} \mathbf{b} \approx \begin{bmatrix} \mathbf{W_h\, h} \\ \mathbf{l} \end{bmatrix} , \tag{4.2}$$

where $\mathbf{h}$ denotes the high-resolution image, $\mathbf{l}$ is the legacy image, $\mathbf{b}$ is the desired blended image, $\mathbf{W_h}$ and $\mathbf{W_l}$ are the diagonal weighting matrices for the high-resolution and legacy images, respectively, and $\mathbf{S}$ is the non-stationary smoothing specified by equation (4.1). The formal solution of the least-squares problem (4.2) is

$$\mathbf{b} \;=\; \left(\mathbf{W_h}^2 + \mathbf{S}^T\mathbf{W_l}^2\mathbf{S}\right)^{-1} \left(\mathbf{W_h}^2\,\mathbf{h} + \mathbf{S}^T\,\mathbf{W_l}\mathbf{l}\right) . \tag{4.3}$$

Alternatively, equation (4.3) can be rearranged as

$$\begin{aligned} \mathbf{b} \;&=\; \left(\mathbf{W_h}^2 + \mathbf{S}^T\mathbf{W_l}^2\mathbf{S}\right)^{-1} \left(\mathbf{W_h}^2\,\mathbf{h} + \mathbf{S}^T\mathbf{W_l}^2\mathbf{S}\mathbf{h} - \mathbf{S}^T\mathbf{W_l}^2\mathbf{S}\mathbf{h} + \mathbf{S}^T\,\mathbf{W_l}\mathbf{l}\right) \\ &=\; \left(\mathbf{W_h}^2 + \mathbf{S}^T\mathbf{W_l}^2\mathbf{S}\right)^{-1} \left(\left(\mathbf{W_h}^2 + \mathbf{S}^T\mathbf{W_l}^2\mathbf{S}\right)\mathbf{h} + \mathbf{S}^T\mathbf{W_l}\left(\mathbf{l} - \mathbf{W_l}\mathbf{S}\mathbf{h}\right)\right) \\ &=\; \mathbf{h} + \left(\mathbf{W_h}^2 + \mathbf{S}^T\mathbf{W_l}^2\mathbf{S}\right)^{-1} \mathbf{S}^T\,\mathbf{W_l}\left(\mathbf{l} - \mathbf{W_l}\mathbf{S}\mathbf{h}\right) , \end{aligned} \tag{4.4}$$

which makes it evident that the merged image is simply the high-resolution image with some changes.

The weights, $\mathbf{W_h}$ and $\mathbf{W_l}$, are applied to the images to bring out the desired qualities from each image. For example, because we prefer the high-resolution image in the shallow section, we weight it more significantly there and gradually taper the weight to preference the legacy image with depth. In addition, we estimate the

legacy weight, $\mathbf{W_l}$, to balance the legacy image's amplitudes with respect to the high-resolution image. The specific values we used for the weights are shown in Figure 4.3.

We implement the inversion in equation (4.4) iteratively using the method of conjugate gradients (Hestenes and Stiefel, 1952). The resultant blended image, shown in Figure 4.1(c), retains the higher frequencies from the high-resolution image while incorporating the lower frequencies from the legacy image (Figure 4.4). The broader frequency bandwidth corresponds to an increase in resolution and leads to a more detailed and interpretable image. As a result, the blended image resembles the high-resolution image but has a marked decrease in noise and extended coverage with depth.

Although the method presented in this chapter is applied to post-stack images, the general method is likely flexible enough to be extended to pre-stack data. Applications of matching legacy and high-resolution seismic data are also seen in time-lapse image registration, where the accurate interpretation of 4D time-lapse data heavily depends on dataset alignment and uniform processing (Ross and Altan, 1997). The method from this chapter could also be used in 4D time-lapse processing; particularly the steps involving frequency balancing and accounting for time shifts.

P-CABLE EXAMPLE

Our second example refers to data from the inner shelf of the Gulf of Mexico, just off of San Luis Pass, Texas (Meckel et al., 2017). The high-resolution P-cable data set was acquired from a shallow marine environment in the Gulf of Mexico. The area of interest for this survey was the near subsurface, and a high frequency source was

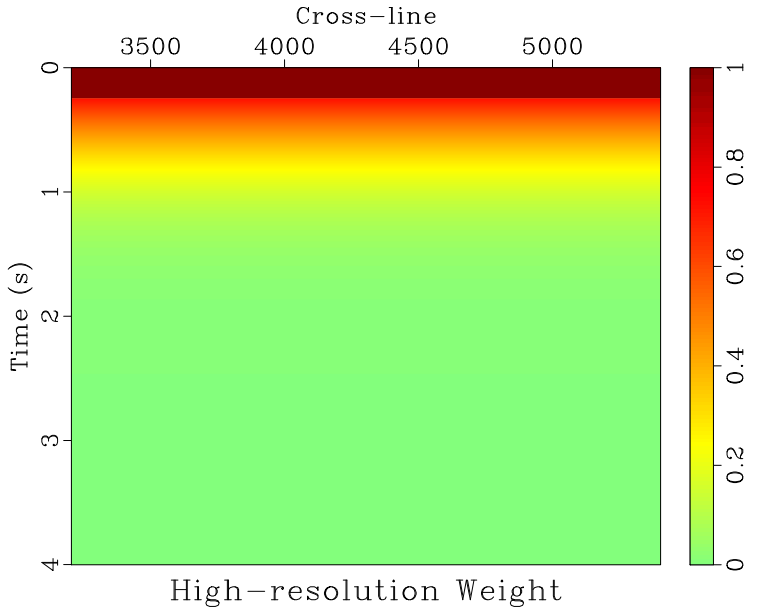

(a)

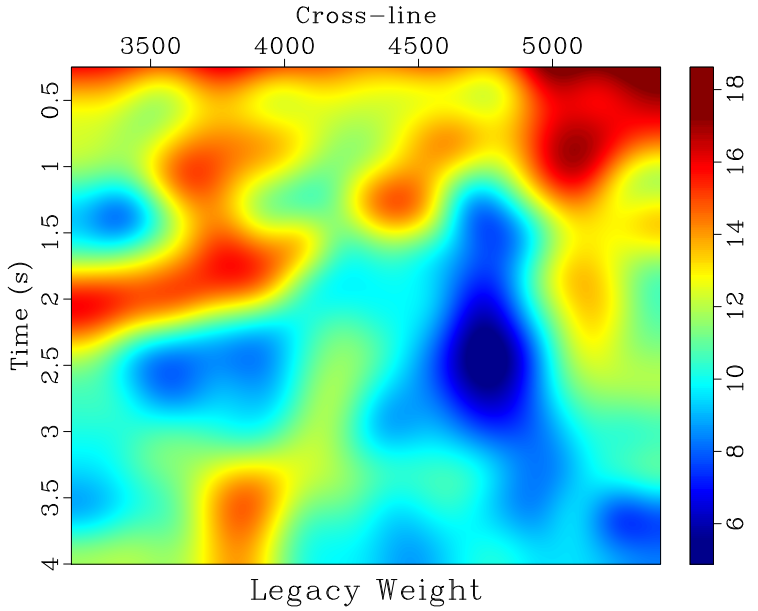

(b)

Figure 4.3: The weights for the high-resolution (a) and legacy (b) images for the least-squares merge. The high-resolution weight is strongly weighted in the shallow part and blends to favor the legacy image with depth. The legacy weight is selected to boost the legacy image's relative amplitudes to match that of the high-resolution image. chapter-merge/apache hweight,lweight-reverse

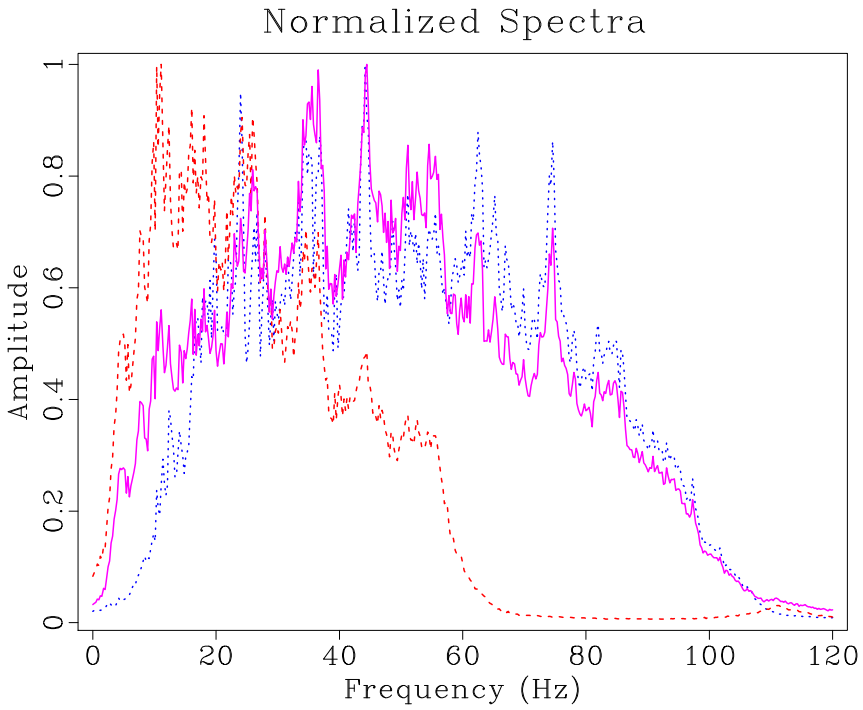

Figure 4.4: The spectra of the entire image display of the legacy (red dashed), high-resolution (blue dotted), and merged (magenta solid) images for the first data set. chapter-merge/apache nspectra22-reverse

used which allows for exceptional resolution in the shallow section, at the expense of less coherent signal information at depth caused by attenuation (Meckel and Mulcahy, 2016). In addition, very little low-frequency information is present in the P-cable data because of the high-frequency source used, which makes balancing spectral content particularly difficult. The other image comes from legacy data coverage over the same area, which has better signal continuity at depth than the high-resolution P-cable data. This is apparent by looking at the first few hundred milliseconds of data for both data sets (Figure 4.5).

Due to the nature of acquisition, the high resolution image has very dense spatial coverage, providing detailed time slices of the near subsurface (Meckel and Mulcahy, 2016). The legacy image has lower spatial resolution. As a result, when matching the high-resolution and legacy images spatially, the high spatial resolution of the high-resolution image must be degraded to match that of the legacy image. We rebinned the legacy and high-resolution images to align them spatially for comparison (Figure 4.7). We chose to spatially down-sample the high-resolution image to match the legacy image as opposed to interpolating the legacy image to the high-resolution image's spatial grid to prevent potentially introducing inaccurate data in the merged image.

There is a definite separation in frequency content when comparing the legacy and high-resolution images (Figure 4.6). Because of little overlap in frequency bandwidth, balancing their spectral content is challenging. In addition, a primary assumption made in deriving the theoretical smoothing radius (equation 4.1) is that the signal is modeled by a summation of Ricker wavelets, which may not be a correct assumption. As a result, additional steps must be taken beyond applying the smoothing specified by equation (4.1) to ensure matching frequency content.

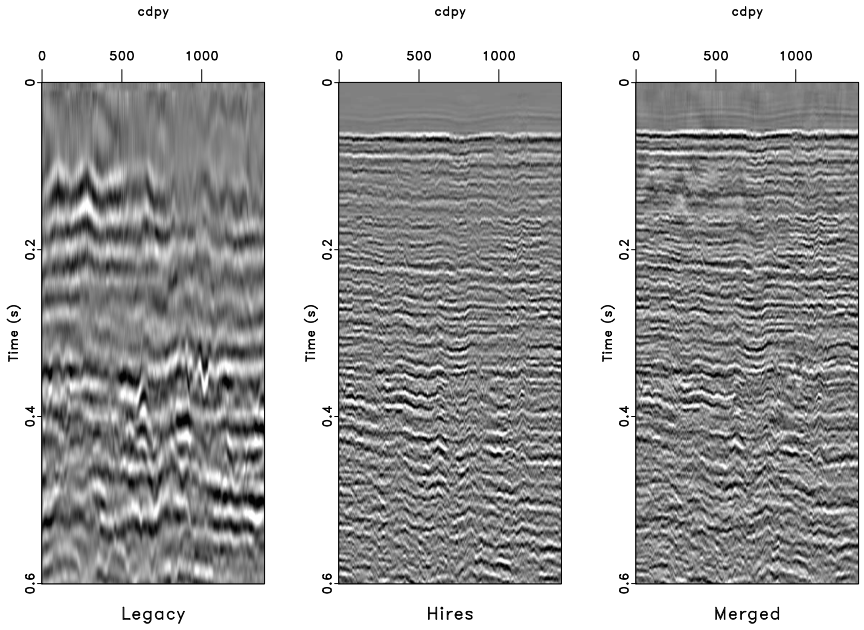

(a)

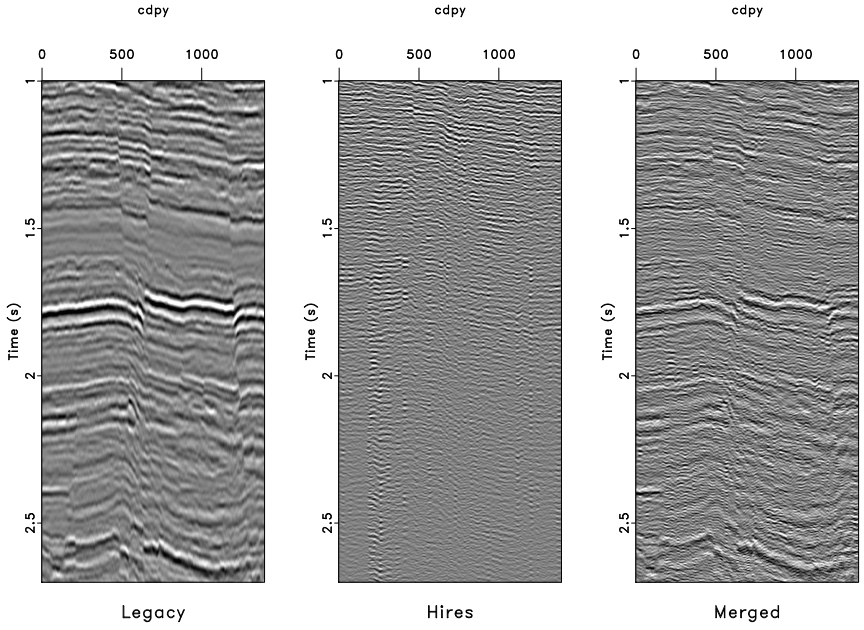

(b)

Figure 4.5: The first 600 ms of data from a sample line from the legacy, high-resolution, and merged image (a). The same images with depth for the legacy, high-resolution, and merged images (b). The merged image resembles the high-resolution image in the shallow parts and incorporates the more coherent lower frequency information from the legacy image with depth. chapter-merge/pcable window1,window2

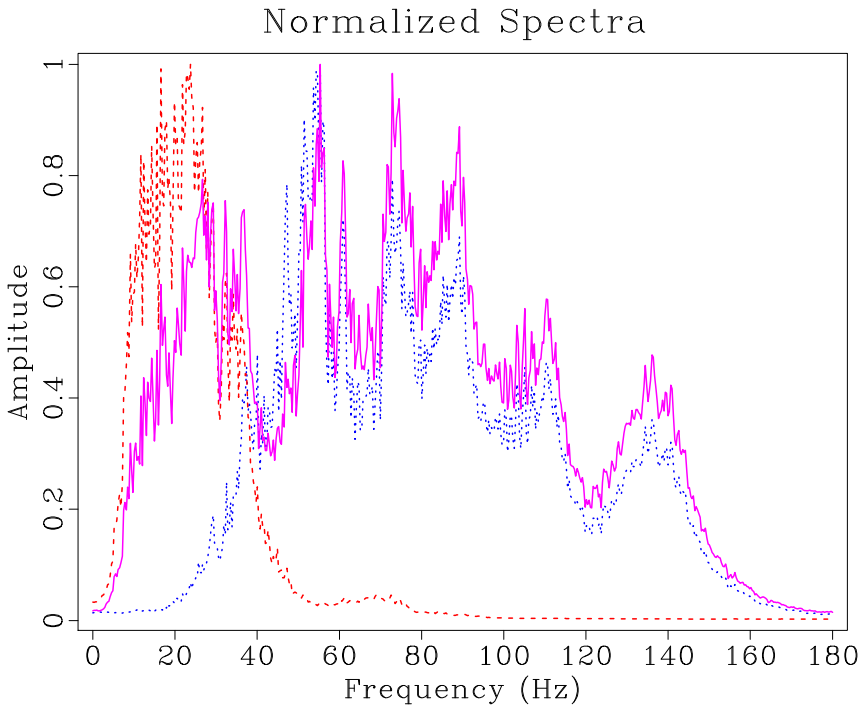

Figure 4.6: The spectral content of the entire image display of the legacy (red dashed), high-resolution (blue dotted), and resultant merged (magenta solid) images for the second data set. chapter-merge/pcable nspectra2

We first apply a low-cut filter to the legacy data to remove the low frequency information that is simply not present in the high-resolution image. Next, we adjust the non-stationary smoothing radius using the simple iterative algorithm (Greer and Fomel, 2017a) that was described in Chapter 3.

After this, we use the low-cut filtered legacy and smoothed high-resolution images to find estimated time shifts we need to apply to the high-resolution image to align the reflections with the legacy image. Then, we apply this estimated time shift to the original high-resolution image and blend it with the original legacy image as specified by equations (4.2) and (4.4).

The resultant merged image is shown in Figure 4.7(c). The frequency content of the merged image is shown in Figure 4.6. Here, the merged image spans the frequency bandwidth of the two initial images, thus producing a high resolution volume including optimal signal characteristics from the two initial images.

CONCLUSIONS

We propose an approach to matching seismic images of different resolutions. Our first step is non-stationary smoothing of the high-resolution image to match the spectral content and amplitudes of the legacy image. Next, we estimate the relative time shifts using local similarity scanning. After matching the two images, we create a blended image by least-squares inversion, which effectively combines the best features of the two images: the broader frequency bandwidth of the high-resolution image with the reflection continuity and deeper coverage of the legacy image. The final result is an interpretable blended image that has higher temporal resolution than either of the two initial images. Two example applications using high-resolution and legacy seismic

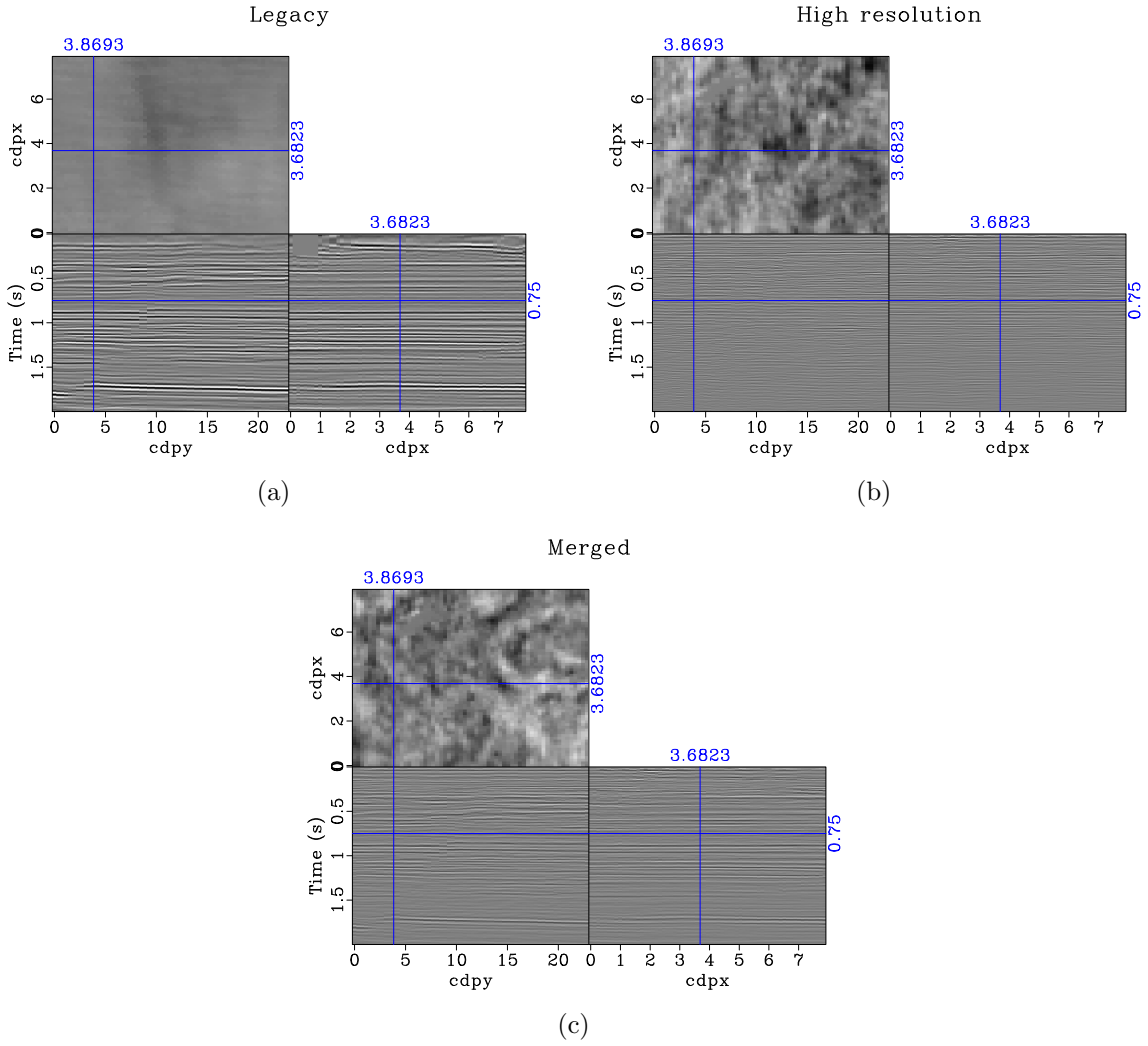

Figure 4.7: The legacy (a), high-resolution (b), and resultant merged (c) images of the second data set. chapter-merge/pcable2 legacy4,hires4,merge3

images from the Gulf of Mexico demonstrate the effectiveness of our method.

ACKNOWLEDGMENTS

We thank Michael DeAngelo, August Lau, Tip Meckel, and Chuan Yin for useful discussions and Apache and Fieldwood for providing the data used in the first example. We also thank the sponsors of the Texas Consortium for Computational Seismology (TCCS) for their financial support.

Chapter 5

Improving migration resolution by approximating the least-squares Hessian using non-stationary amplitude and frequency matching

We propose using two non-stationary operators to represent the amplitude and frequency variations in the least-squares Hessian to account for the principal differences between conventional and least-squares migrated images. The calculation and application of these operators are computationally inexpensive when compared to one iteration of least-squares migration, and it increases the resolution and amplitude fidelity of the migrated image. Successful results are achieved on an application of reverse-time migration to the Sigsbee synthetic data set.

INTRODUCTION

Least-squares migration can produce an accurate migrated seismic image. However, the process may be computationally expensive as it is typically performed in an iterative manner, where each iteration involves forward modeling and migration. Although conventional seismic migration is less computationally expensive than least-squares migration, it generally contains migration artifacts affecting amplitude fidelity and resolution (Dong et al., 2012; Dai and Schuster, 2013). This can be attributed to the

Parts of this chapter were first published in Greer et al. (2018). This work was done under the supervision of Dr. Sergey Fomel, and Dr. Zhiguang Xue assisted in the migration of the Sigsbee synthetic data set.

fact that, while least-squares migration inverts for subsurface reflectivity by finding the least-squares model solution, standard migration amounts to applying a single adjoint operation (Claerbout, 1992).

Various methods have attempted to correct these differences by finding and applying an approximation to the inverse Hessian operator, $\mathbf{H}^{-1} = \left(\mathbf{L}^{\mathsf{T}}\mathbf{L}\right)^{-1}$, to a conventional migrated image. Here, $\mathbf{L}$ is a standard forward-modeling operator, and $\mathbf{L}^{\mathsf{T}}$ is its adjoint—the migration operator. These methods usually take the form of two approaches—for preconditioning before least-squares migration and as a single operation to improve accuracy of a conventionally migrated image. Previously, this has been done by migration deconvolution (Hu et al., 2001; Yu et al., 2006), approximating the diagonal of $\mathbf{H}^{-1}$ to account for amplitude effects (Rickett, 2003; Sacchi et al., 2007), and by finding and applying a bank of non-stationary matching filters (Guitton, 2004, 2017) or deblurring filters (Aoki and Schuster, 2009) to a conventionally migrated image. This traditionally is done using a sliding window approach, where windowed regions and partial overlap regions are specified, and different matching filters are specified in each region (Schuster, 2017).

In this thesis, we take a different approach. We note that the two primary differences between least squares migrated images and conventional migrated images are amplitude and frequency variations (Hou and Symes, 2015, 2016). Here, we treat this as a data matching problem between two conventionally migrated images, and find separate operations to account for both amplitude and frequency variations.

This approach enables us to rely on local seismic attributes to measure and apply amplitude and frequency balancing operations instead of using a sliding window approach (Fomel, 2007a). This allows for the smooth estimation and application of

these matching operations instead of applying them in discrete windows. Because the operations for balancing amplitude and frequency content are calculated and applied separately from each another, the effect of each operation can be adjusted independently, which is another advantage of the proposed method. To test the proposed approach, we apply this method to an example of reverse-time migration on the Sigsbee synthetic data set (Paffenholz et al., 2002).

THEORY

The goal of least-squares migration is to find the image, $\hat{\mathbf{r}}$, that minimizes

$$p(\hat{\mathbf{r}}) = \frac{1}{2} \left\| \mathbf{d} - \mathbf{L}\hat{\mathbf{r}} \right\|_2^2 \ , \tag{5.1}$$

where $\mathbf{L}$ is the forward modeling operator, representing seismic wave propagation through the subsurface, and $\mathbf{d}$ is the acquired seismic data. This can be solved by the least-squares formulation to find $\hat{\mathbf{r}}$:

$$\hat{\mathbf{r}} = \left(\mathbf{L}^\mathsf{T}\mathbf{L}\right)^{-1} \mathbf{L}^\mathsf{T}\mathbf{d} \ , \tag{5.2}$$

where the migration operator, $\mathbf{L}^\mathsf{T}$, is adjoint to the forward modeling operator and is typically sparse, and $\left(\mathbf{L}^\mathsf{T}\mathbf{L}\right)^{-1}$ is the inverse Hessian operator. Equation (5.2) is usually solved iteratively, typically requiring multiple iterations of forward modeling and remigrating the seismic image (Kuehl and Sacchi, 2003; Xue et al., 2016). Conventional migration is less computationally expensive:

$$\mathbf{m}_0 = \mathbf{L}^\mathsf{T}\mathbf{d}. \tag{5.3}$$

However, conventionally migrated images generally exhibit less correct amplitude and frequency content than least-squares migrated images (Dutta et al., 2014). By

combining equations (5.2) and (5.3), it is evident that

$$\hat{\mathbf{r}} = \left(\mathbf{L}^{\mathsf{T}}\mathbf{L}\right)^{-1}\mathbf{m}_0 \,, \tag{5.4}$$

so $\mathbf{m}_0$ is a distorted version of $\hat{\mathbf{r}}$, and $\hat{\mathbf{r}}$ can be recovered from $\mathbf{m}_0$ by finding a good approximation of $\left(\mathbf{L}^{\mathsf{T}}\mathbf{L}\right)^{-1}$.

METHOD

In order to approximate $\left(\mathbf{L}^{\mathsf{T}}\mathbf{L}\right)^{-1}$, we follow the modeling and remigration process of Guitton (2004). We begin by forward modeling the migrated image, $\mathbf{m}_0$:

$$\mathbf{d}_1 = \mathbf{L}\mathbf{m}_0 \,. \tag{5.5}$$

We then remigrate $\mathbf{d}_1$:

$$\mathbf{m}_1 = \mathbf{L}^{\mathsf{T}}\mathbf{d}_1 = \left(\mathbf{L}^{\mathsf{T}}\mathbf{L}\right)\mathbf{m}_0 \,, \tag{5.6}$$

and then find the operator, $\left(\mathbf{L}^{\mathsf{T}}\mathbf{L}\right)^{-1}$, that satisfies

$$\mathbf{m}_0 = \left(\mathbf{L}^{\mathsf{T}}\mathbf{L}\right)^{-1}\mathbf{m}_1 \,. \tag{5.7}$$

Therefore, the inverse Hessian operator, $\mathbf{H}^{-1} = \left(\mathbf{L}^{\mathsf{T}}\mathbf{L}\right)^{-1}$, that must be applied to $\mathbf{m}_0$ to obtain $\hat{\mathbf{r}}$ can be calculated by first finding the transformation, $\mathbf{H}$, that maps $\mathbf{m}_0$ to $\mathbf{m}_1$, and then inverting it. This can be interpreted as a data matching problem between $\mathbf{m}_1$ and $\mathbf{m}_0$.

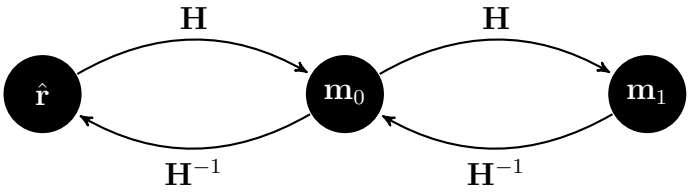

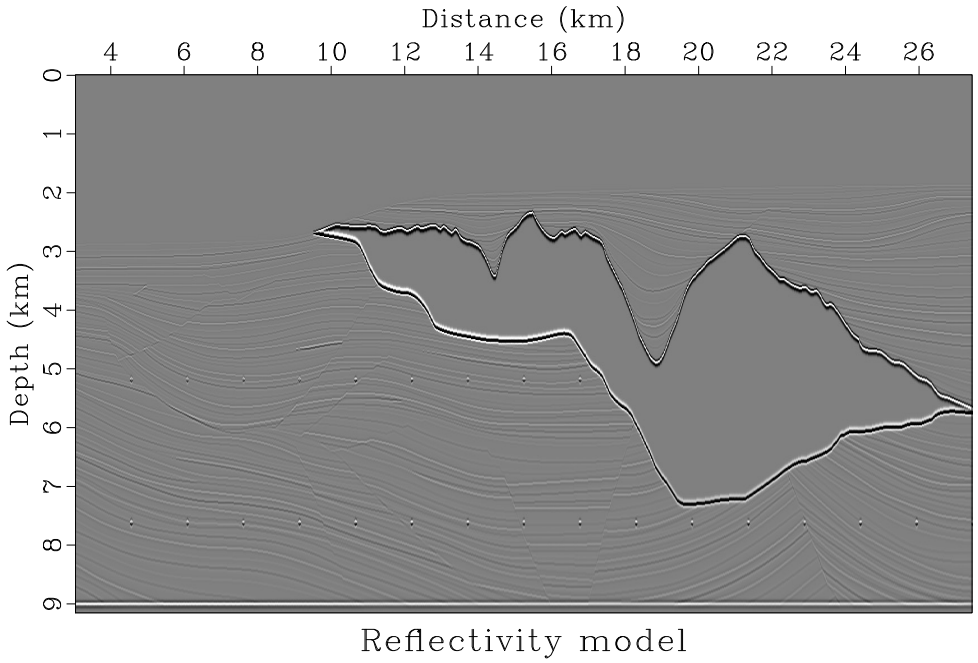

(a)

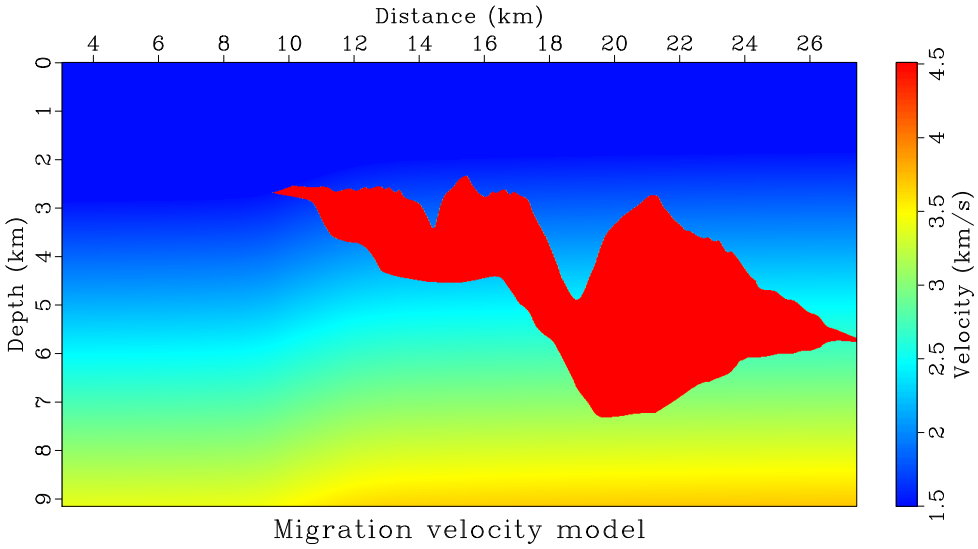

(b)

Figure 5.1: The Sigsbee model reflectivity (a), and migration velocity model (b). chapter-mighes/sigsbee mod,vel-migration

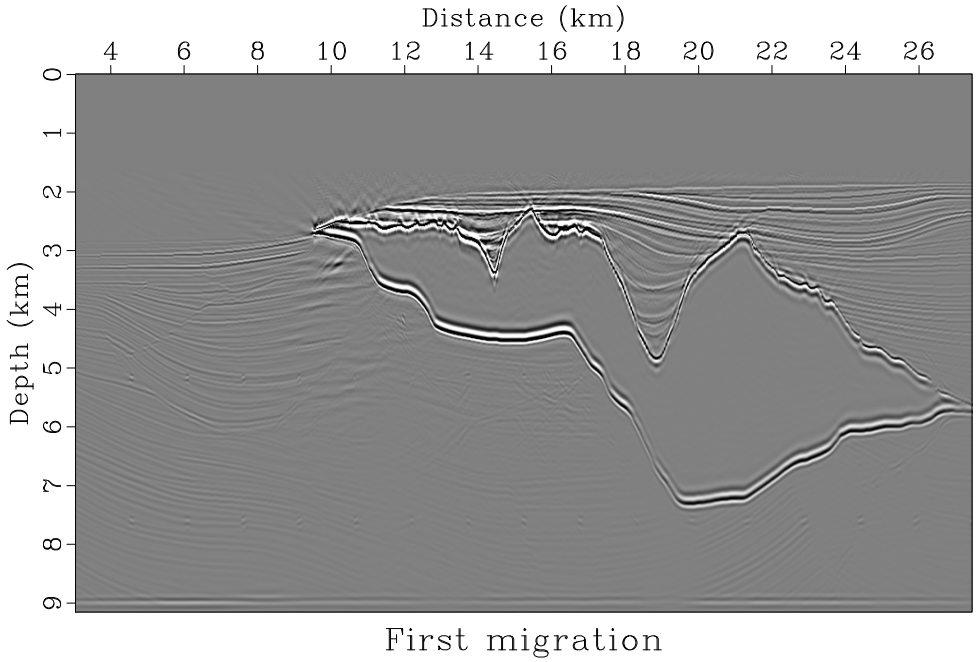

(a)

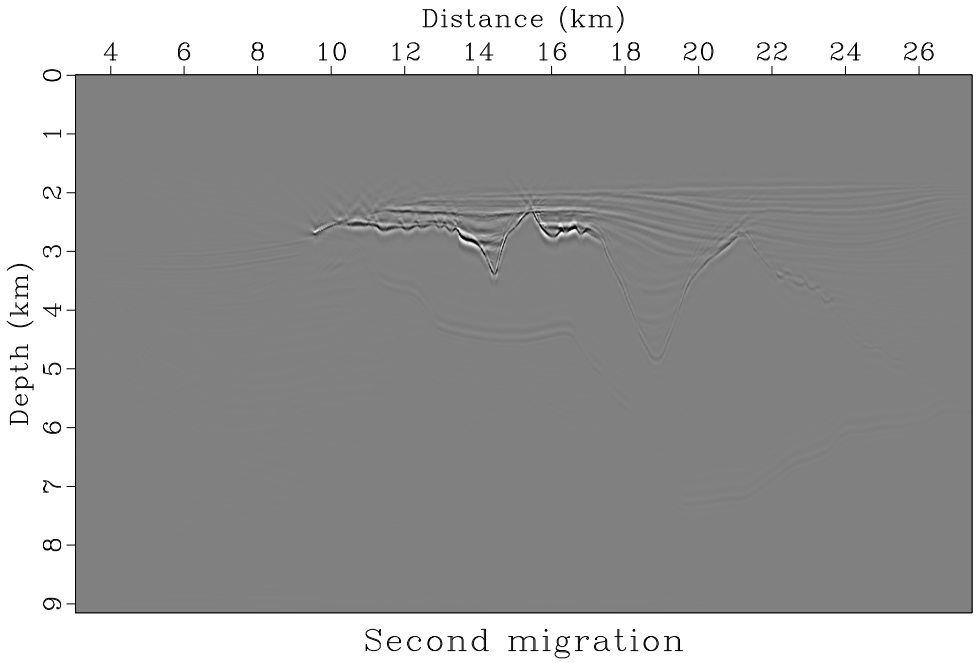

(b)

Figure 5.2: The first migrated image, $\mathbf{m}_0$ (a), and the second migrated image, $\mathbf{m}_1$ (b). chapter-mighes/sigsbee image0,image1

Because the primary differences between conventionally migrated images and least-squares migrated images amount to amplitude and frequency variations, we use two separate non-stationary operators to represent the forward Hessian—one to account for amplitude variations, and the other to account for frequency variations. Therefore, our approximation of $\mathbf{H}$ can be calculated from some application of a non-stationary amplitude balancing operator, $\mathbf{A}$, and a non-stationary frequency balancing operator, $\mathbf{S}$. We first calculate the forward Hessian because the forward frequency balancing operation, $\mathbf{S}$, is well defined and simple to calculate. We then invert our approximation to the Hessian and apply it to $\mathbf{m}_0$ to correct the amplitude and frequency content of the migrated image.

Amplitude operator

First, we choose to find an amplitude balancing operation that, when applied to $\mathbf{m}_0$, balances the amplitudes of $\mathbf{m}_0$ with respect to $\mathbf{m}_1$. This operation can be equated to a trace-by-trace multiplication of a diagonal matrix to each trace, where the matrix changes for every trace. We estimate it by first calculating the amplitude envelope of the traces in $\mathbf{m}_0$ and $\mathbf{m}_1$, and then smoothly dividing them. The corresponding diagonal weighting operator, $\mathbf{A}$, can be applied such that $\mathbf{m}_1 \approx \mathbf{A}\mathbf{m}_0$ to balance the amplitudes of each trace. Because this is a linear operation that only has diagonal elements, finding the inverse operator, $\mathbf{A}^{-1}$ is trivial.

Frequency operator

In addition to amplitude corrections, we also attempt to account for the decrease in resolution of a conventional migrated image compared to its corresponding least-squares migrated image. This loss in resolution can be equated to the fact that

$\mathbf{L}^\mathsf{T}\mathbf{L}$ acts as a blurring operator, where the conventional migrated image is a blurred version of the ideal least-squares migrated image (Hu et al., 2001). We choose to approximate this blurring using non-stationary triangle smoothing.

We begin by first calculating the local frequency of the two initial images (Fomel, 2007a). Local frequency is a temporally and spatially varying frequency attribute that smoothly varies across the image without windows. Our goal is to find a transformation that we can apply to $\mathbf{m}_0$ that matches the local frequency content with $\mathbf{m}_1$. To do this, we propose using non-stationary triangle smoothing. This approach involves finding and applying a non-stationary smoothing operator, which is the number of samples, in both dimensions, that $\mathbf{m}_0$ will be averaged over in a triangle weight, to balance the local frequency content with $\mathbf{m}_1$.

We find the smoothing radius iteratively using the method of Greer and Fomel (2017a) from Chapter 3, with a modification that allows the smoothing radius to be calculated in both spatial directions. Essentially, this is found by choosing an initial guess of a smoothing radius, $\mathbf{R}^{(0)}$, and updating it iteratively such that

$$\mathbf{R}^{(i+1)} = \mathbf{R}^{(i)} + \alpha \left[\mathbf{F}[\mathbf{S}_{\mathbf{R}^{(i)}}\mathbf{m}_0] - \mathbf{F}[\mathbf{m}_1]\right] \ , \tag{5.8}$$

where $\mathbf{F}$ is the local frequency operator, $\mathbf{S}_{\mathbf{R}^{(i)}}$ is the smoothing operator of radius $\mathbf{R}$ at the ith iteration, and α is a scalar constant that represents the step length. After a small number of iterations, the smoothing operator is found that, once applied to $\mathbf{m}_0$, balances local frequency content with $\mathbf{m}_1$.

For this particular application using depth migration, this operator should technically be specified to balance *wavenumber* instead of *frequency*. However, it is kept as frequency to keep consistent terminology with the algorithm developed in Chapter 3.

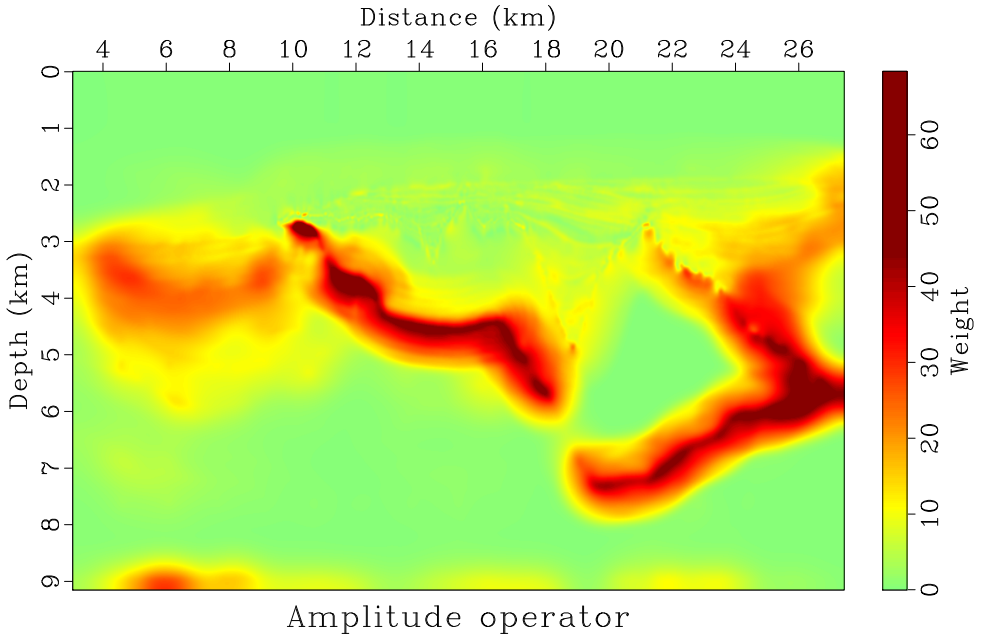

(a)

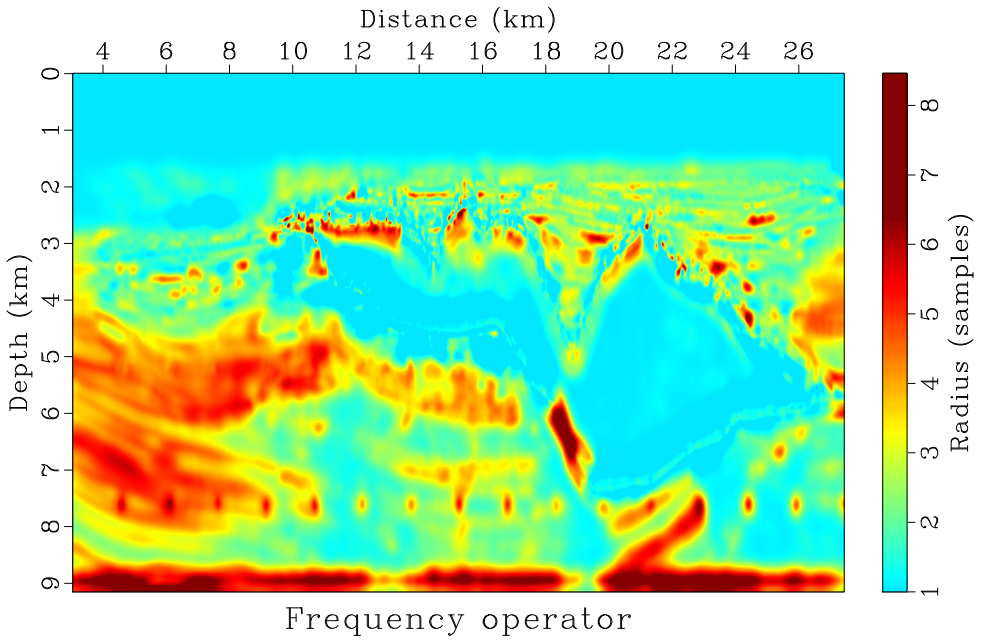

(b)

Figure 5.3: The forward amplitude balancing weight, **A** (a) and the smoothing radius (b), which represents the number of samples in both dimensions that $\mathbf{m}_0$ must be smoothed over in a triangle weight to balance the local frequency content with $\mathbf{m}_1$. This represents the forward smoothing operation, **S**. chapter-mighes/sigsbee a0,rect10b

Calculating the inverse Hessian

Now that we have found the forward operators that separately balance amplitude and frequency content from $\mathbf{m}_0$ to $\mathbf{m_1}$, where $\mathbf{m}_1 \approx \mathbf{H}\mathbf{m}_0$, we want to find what combination of $\mathbf{A}$ and $\mathbf{S}$ best approximates $\mathbf{H}$. Since $\mathbf{H} = \mathbf{L}^\mathsf{T}\mathbf{L}$ is symmetric, we want our approximation of $\mathbf{H}$ to be as close to symmetric as possible. Therefore, we define $\mathbf{H}$ as

$$\mathbf{H} \approx \mathbf{A}^{1/2}\mathbf{S}\mathbf{A}^{1/2} \,, \tag{5.9}$$

where $\mathbf{A}$ is the operator that balances the amplitudes of $\mathbf{m}_0$ with respect to $\mathbf{m}_1$, and $\mathbf{S}$ is the operator that balances the local frequency content of $\mathbf{m}_0$ with respect to $\mathbf{m}_1$, both defined previously. Applying the operations in this order allows the approximation of $\mathbf{H}$ to be symmetric because both $\mathbf{A}$ and $\mathbf{S}$ are symmetric operations. Splitting up our approximation to the Hessian into two separate operators allows us to control how much of each operation and the order of each operation goes into correcting the image, and see how it affects the resulting image. Now that we have found the forward Hessian, $\mathbf{H}$, such that $\mathbf{H}\mathbf{m}_0 \approx \mathbf{m}_1$ using data matching operators, we want to find the inverse of this operator, $\mathbf{H}^{-1}$, such that $\hat{\mathbf{r}} \approx \mathbf{H}^{-1}\mathbf{m}_0$ provides us with the least-squares image. This is found as

$$\mathbf{H}^{-1} \approx \left(\mathbf{A}^{1/2}\mathbf{S}\mathbf{A}^{1/2}\right)^{-1} = \mathbf{A}^{-1/2}\mathbf{S}^{-1}\mathbf{A}^{-1/2} \,. \tag{5.10}$$

Because the amplitude operators only contain diagonal terms, they are simple to invert. However, $\mathbf{S}^{-1}$ is non-trivial to calculate since inverse smoothing can create physically unrealistic high-frequency data if inverted incorrectly without regularization.

Figure 5.4 shows transfer functions for a stationary forward and inverse triangle smoothing operator of a radius of 10 samples. In the forward case, triangle

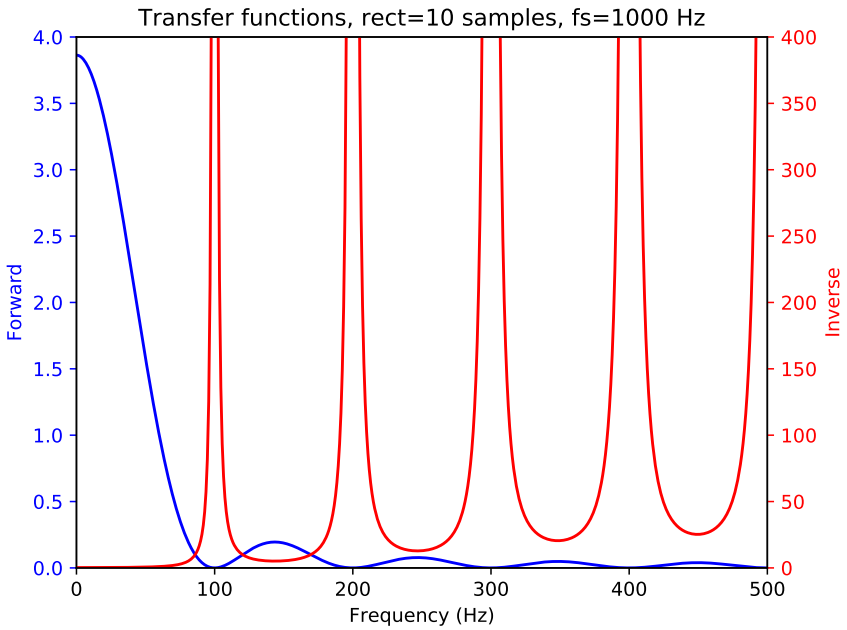

Figure 5.4: Transfer functions for a stationary forward triangle smoothing operator (blue) and its inverse (red). chapter-mighes/triop tf

smoothing acts as a low-pass filter. However, its inverse can introduce high frequency information, which is physically unrealistic for the data we are working with.

Therefore, $\mathbf{S}^{-1}$ must be calculated with care to ensure the inverted data is physically plausible. We iteratively invert $\mathbf{S}$ using shaping regularization (Fomel, 2007b), where the shaping operator is a bandpass filter picked to ensure the passband contains only physically possible frequencies for the given data set. The cost of applying our approximation to $\mathbf{H}^{-1}$ in equation (5.10) is $\mathcal{O}(N)$, where N is the image size. The constant is small, typically around 10 for the number of iterations, and the calculation and application of this approximation is computationally insignificant compared to one iteration of least-squares migration.

EXAMPLE

We demonstrate the effectiveness of this method on the 2D Sigsbee model. The Sigsbee2A 2D synthetic data set was created to mimic the geology of the Sigsbee escarpment in the Gulf of Mexico (Paffenholz et al., 2002). A fixed-spread acquisition survey is generated, which consists of 301 shots spaced every 122 m. The source wavelet for generating the synthetic data is a Ricker wavelet centered at 10 Hz. The record length of the synthetic data is 10 s with a sampling interval of 4 ms. We use reverse-time migration (RTM) as our migration operator.

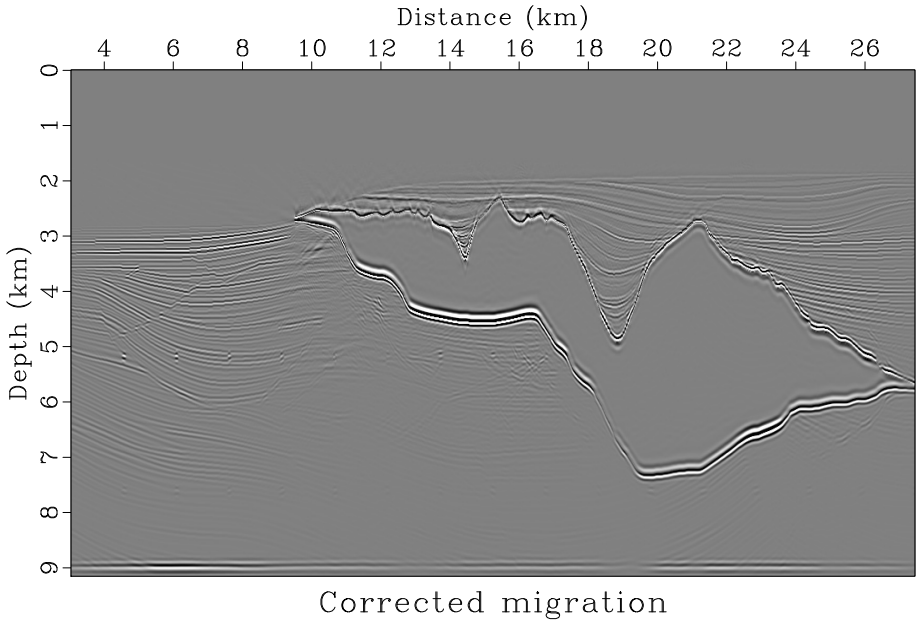

Figure 5.5: The corrected migrated image, found by applying equation (5.10) to $\mathbf{m}_0$. chapter-mighes/sigsbee migdec-shap

We begin with the sub-surface reflectivity model (Figure 5.1(a)) and migration velocity model (Figure 5.1(b)). Next, we forward model the seismic data and migrate it to obtain our first conventionally migrated image, $\mathbf{m}_0$ (Figure 5.2(a)). Then, we forward model $\mathbf{m}_0$ and remigrate that data to obtain $\mathbf{m}_1$ (Figure 5.2(b)). This pro-

vides us with the two images, $\mathbf{m}_0$ and $\mathbf{m}_1$, that we can use to find the operation $\mathbf{H}$ that maps $\mathbf{m}_0$ to $\mathbf{m}_1$.

Next, we calculate and apply the data matching operations as described in the previous section. The forward amplitude balancing weight, $\mathbf{A}$, is shown in Figure 5.3(a). The calculated radius for the forward smoothing operation is shown in Figure 5.3(b). After applying these two operators to $\mathbf{m}_0$ as described by equation (5.10), we produce the corrected migrated image, as shown in Figure 5.5. This corrected image better represents the subsurface reflectivity than the conventionally migrated image (Figure 5.2(a)), as it exhibits more correct amplitude content and higher resolution comparable with the reflectivity model.

Figure 5.6 shows a windowed section of the reflectivity model, the conventionally migrated image, and the corrected migrated image. The corrected migrated image exhibits clearly higher resolution and has more correct and consistent amplitude content than the conventionally migrated image.

In addition to directly applying this operator to the conventionally migrated image to improve resolution, this operator can be used as a preconditioner in iterative least-squares migration. In this case, the corrected migrated image could be used as an initial model for least-squares migration for faster convergence.

CONCLUSIONS

Least-squares migration can produce an accurate migrated image, but it is more computationally expensive than conventional migration. In this chapter, we apply an approximate inverse Hessian operator to a conventional migrated image to approximate the least-squares migrated image. Because the primary differences between

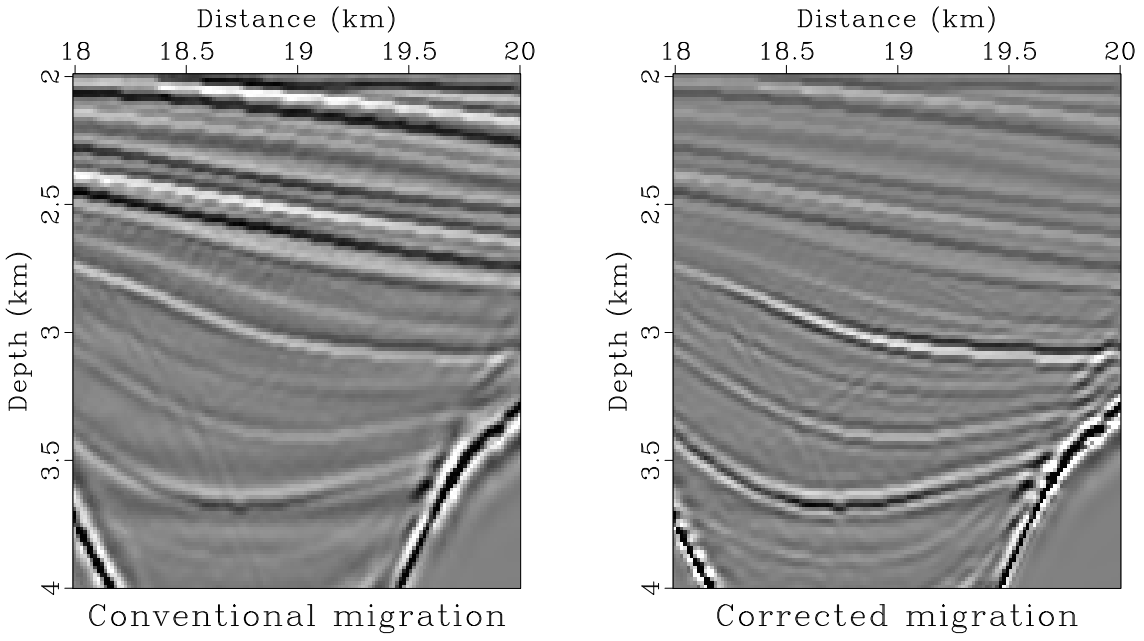

(a)

(b)

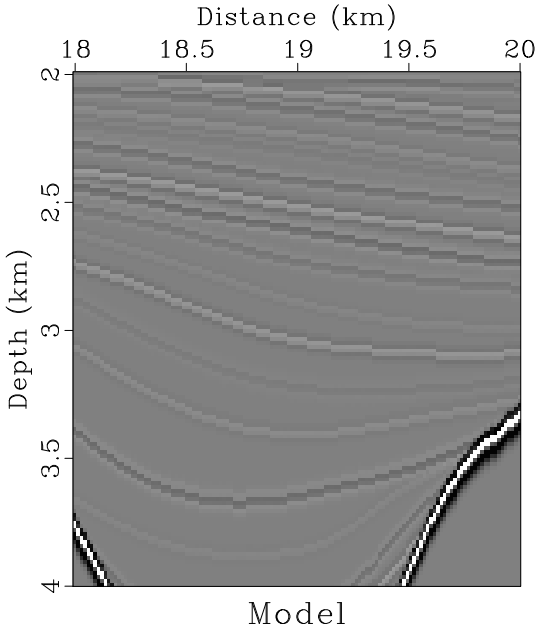

(c)

Figure 5.6: The first migrated image (a), the corrected migrated image (b), and the Sigsbee model reflectivity (c). chapter-mighes/sigsbee image0-w3,migdec-w3,mod-w3

least-squares migration and conventional migration amount to amplitude and frequency variations, we approximate the forward Hessian by calculating frequency and amplitude matching operators. The amplitude matching operator is found by calculating the amplitude envelopes of migrated and remigrated images and smoothly dividing them, and the frequency matching operator is found using an iterative algorithm and non-stationary smoothing. The Hessian is approximated by a combination of these two operators to ensure symmetry. This method involves a windowless approach and is cheap to calculate and apply. Additionally, by defining the Hessian with two separate operators, we can examine, and control, the "ingredients" of the Hessian operator, and see how changing them impacts the final image.

After the forward Hessian is calculated, we invert it iteratively using shaping regularization, and apply it to the conventionally migrated image to get an approximation of the least-squares migrated image. Successful results are achieved on the 2D Sigsbee synthetic model with reverse-time migration as the migration operator.

ACKNOWLEDGMENTS

We thank the sponsors of the Texas Consortium for Computational Seismology (TCCS) for their financial support. The examples in this chapter can be reproduced using the Madagascar open-source software package (Fomel et al., 2013).

Chapter 6

Conclusions

In this thesis, I discussed several methods and applications of data matching in seismic data analysis. Chapter 2 introduced on introducing the three data matching operators that are used in this thesis—shifting, scaling, and filtering. Chapter 3 introduced different methods of frequency balancing using non-stationary smoothing. The first method to find the non-stationary smoothing *radius*, or number of samples each data point is averaged over with a triangle weight, took a theoretical approach based on the assumption that the data we observe can be represented by a superposition of Ricker wavelets. This method worked well in certain situations, but was not robust enough to work for all of the given data sets. In the second method, I introduced an iterative algorithm to find the smoothing radius. In my experiments, this method converges quickly and works well in several presented situations. Finally, a modification to this algorithm was shown that allows adaptive smoothing for more complex data sets.

This chapter also discussed two applications of these algorithms. The frequency balancing algorithm was demonstrated on an application to matching high-resolution and legacy seismic images, and the modified algorithm was demonstrated on an application to multicomponent seismic image registration.

Chapter 4 went into more detail of the application of matching and merging high-resolution and legacy seismic images. This example takes two seismic volumes,

acquired over the same area but using different technologies, and first matches them before merging them together to produce an optimized third image. First, I demonstrated the method on a 2D line from the Gulf of Mexico. Then, I applied the method to a 3D seismic volume from a different part of the Gulf of Mexico.

Chapter 5 discusses another application of improving migration resolution by approximating the least-squares Hessian using non-stationary data matching operations. I showed that an approximation to the least-squares Hessian can be calculated by solving a data matching problem between two conventionally migrated images, and the Hessian can be represented by the combination of amplitude and frequency balancing operations. I applied the proposed approach to a 2D synthetic Sigsbee data set, a traditional benchmark for imaging algorithms.

FUTURE WORK

In the future, the work presented in Chapter 5 should be extended to involve real data and 3D examples. It could also benefit from comparing the results of the proposed approach to previous approaches presented to approximate the least-squares Hessian (Hu and Schuster, 1998; Hu et al., 2001; Yu et al., 2006; Sacchi et al., 2007; Aoki and Schuster, 2009; Dong et al., 2012; Dai and Schuster, 2013; Casasanta et al., 2017), to see how it compares in different situations.

Another extension of this data matching procedure may be to incorporate the phase of the signal to be matched. Negligible improvements were made when trying to incorporate phase corrections into the high-resolution and legacy data matching problem of Chapter 4. However, other data matching problems could benefit from these corrections.

The newly developed field of deep learning may also benefit from including these data matching techniques in the parameterization, as specifically tailoring the neural networks to work with geophysical data in this manner may produce better results.

Several applications of data matching were discussed in this thesis. However, many applications remain unaddressed from a data matching standpoint. Problems such as seismic and well-log tying, deconvolution, automatic gain control (AGC), and surface-related multiple elimination (SRME) can also be recast as data matching problems. Looking at these problems in a new light may bring advancements to computational geophysics.

Appendix

CODE

The examples in this thesis were implemented using the Madagascar open-source software environment for reproducible computational experiments (Fomel et al., 2013). The package is available at `http://www.ahay.org/`.

The reproducible document for the results in this thesis, including code, is available at `http://www.sygreer.com/research/honorsThesis`. However, some of the data used in this thesis are proprietary, so those results may not be directly reproducible.

For brevity in this thesis, code is only included for one example of the main frequency balancing algorithm presented in Chapter 3. The code for the rest of the examples in this thesis are available online at the URL above.

Table 1: List of figures in this thesis and the locations of scripts and programs to generate them

Figures	**Directory**	**Listings**
2.1	chapter-locfreq/merge/	1, 2, 3
2.2, 2.3	chapter-background/dmExample/	—
3.1, 3.2, 3.3, 3.4	chapter-merge/apache/	—
3.5, 3.6, 3.7, 3.8	chapter-locfreq/merge/	1, 2, 3
3.9, 3.10	chapter-locfreq/vecta/	—
3.11	chapter-locfreq/convergence/	—
4.1, 4.2, 4.3, 4.4	chapter-merge/apache/	—
4.5, 4.6	chapter-merge/pcable/	—
4.7	chapter-merge/pcable2/	—
5.1, 5.2, 5.3, 5.5, 5.6	chapter-merge/mighes/	—
5.4,	chapter-merge/triop/	—

Listing 1: chapter-locfreq/merge/SConstruct

```
from rsf.proj import *
from radius import radius

# must have 'legacy.rsf' and 'hires.rsf' initial data sets in same directory

# Initial figures
```

```
Result('legacy','grey title="Legacy"')
Result('hires-agc','hires',
       'agc rect1=2000 rect2=5 | grey title="High-resolution"')

# frequency content
Flow('legacy-spec','legacy','spectra all=y')
Result('nspectra-orig','high-spec legacy-spec',
     '''cat axis=2 ${SOURCES[1]} | scale axis=1 | window max1=180 |
        graph title="Normalized Spectra" label2="Amplitude" unit2=""''')

# Balance local frequency
flol=40
corrections = 5
Flow('legacyfilt','legacy','bandpass flo=%d '%(flol))
radius('hires','legacyfilt', corrections, [0.13,0.2,0.3,0.5,0.5],
       bias=0, clip=90, rect1=80, rect2=16, maxval=90 )

End()
```

Listing 2: chapter-locfreq/merge/radius.py

```
from rsf.proj import *

def radius(high, low,               # initial high and low frequency images
           niter,                   # number of corrections
           c,                       # 'step length' for radius corrections. Can
                                    #       be type int or float for constant c
                                    #       or type array for changing c.
           bias=-15, clip=30,       # bias and clip for display
           rect1=40, rect2=80,      # radius for local frequency calculation
           maxrad=1000,             # maximum allowed radius
           theor=True,              # use theoretical smoothing radius
           scale=9,                 # scale for theoretical smoothing radius
           initial=10,              # initial value for contant smoothing radius
           minval=0, maxval=25,     # min and max local frequency for display
           titlehigh="Hires",
           titlelow="Legacy"):

    if type(c) is float or type(c) is int:
        c = [c]*niter

    # plot image
    def seisplot(name):
        return 'grey title="%s"'%name

    # local frequency
    locfreq = '''iphase order=10 rect1=%d rect2=%d hertz=y complex=y |
                 put label="Frequency" unit=Hz'''%(rect1,rect2)

    def locfreqplot(name):
        return 'grey mean=y color=j scalebar=y title="%s" '%name

    # difference in local frequencies
    freqdif = 'add scale=-1,1 ${SOURCES[1]} | put label=Frequency'

    def freqdifplot(num):
        return '''grey allpos=y color=j scalebar=y mean=y
                  title="Difference in Local Frequencies %s"
                  clip=%d bias=%d minval=%d
                  maxval=%d''' %(num,clip,bias,minval,maxval)

```

```
    # plot spectral content
42  specplot = '''cat axis=2 ${SOURCES[1]} |
                scale axis=1 | window max1=180 |
44              graph title="Normalized Spectra" label2="Amplitude" unit2=""'''

46  # plot smothing radius
    def rectplot(name):
48      return '''grey color=j mean=y title="%s" scalebar=y barlabel=Radius
                barunit=samples'''%name
50
    # smooth with radius
52  smooth = 'nsmooth1 rect=${SOURCES[1]}'

54  ##############################################################################

56  # plot images
    Result(high, seisplot(titlehigh))
58  Result(low, seisplot(titlelow))

60  # initial local frequency
    Flow('high-freq',high,locfreq)
62  Result('high-freq',locfreqplot('%s Local Frequency'%titlehigh))

64  Flow('low-freq',low,locfreq)
    Result('low-freq',locfreqplot('%s Local Frequency'%titlelow))
66
    # initial difference in local frequency
68  Flow('freqdif','low-freq high-freq',freqdif)
    Result('freqdif',freqdifplot(''))
70
    # initial smoothing radius
72  if (theor):
        from math import pi
74      Flow('rect0','low-freq high-freq','''math f1=${SOURCES[1]}
        output="sqrt(%g*(1/(input*input)-1/(f1*f1)))/%g"'''%(scale,2*pi*0.001))
76  else:
        Flow('rect0','low-freq','math output=%f'%initial)
78
    Result('rect0',rectplot("Smoothing Radius 0"))
80
    # smoothing using intial smoothing radius guess
82  Flow('high-smooth0','%s rect0' % high,smooth)
    Result('high-smooth0', seisplot("%s Smooth 0"%titlehigh))
84
    # frequency spectra
86  Flow('high-spec',high,'spectra all=y')
    Flow('low-spec',low,'spectra all=y')
88  Flow('high-smooth-spec0','high-smooth0','spectra all=y')
    Result('nspectra','high-spec low-spec',specplot)
90  Result('high-smooth-spec0','high-smooth-spec0 low-spec',specplot)

92  Flow('high-smooth-freq0','high-smooth0',locfreq)
    Result('high-smooth-freq0',
94          locfreqplot("%s Local Frequency Smoothed %d" %(titlehigh,0)))

96  Flow('freqdif-filt0','low-freq high-smooth-freq0',freqdif)
    Result('freqdif-filt0',freqdifplot('0'))
98
    prog=Program('radius.c')
100 for i in range(1, niter+1):
        j = i-1
```

```
102
        # update smoothing radius
104     Flow('rect%d'%i,'rect%d freqdif-filt%d %s'%(j,j,prog[0]),
            './${SOURCES[2]} freq=${SOURCES[1]} c=%f'%c[j])
106     Result('rect%d'%i,rectplot("Smoothing Radius %d")%i)

108     # smooth image with radius
        Flow('high-smooth%d'%i,'%s rect%d'%(high,i),smooth)
110     Result('high-smooth%d'%i, seisplot('%s Smooth %d'%(titlehigh,i)))

112     # smoothed spectra
        Flow('high-smooth-spec%d'%i,'high-smooth%d'%i,'spectra all=y')
114     Result('high-smooth-spec%d'%i,'high-smooth-spec%d low-spec'%i,specplot)

116     # smoothed local frequency
        Flow('high-smooth-freq%d'%i,'high-smooth%d'%i,locfreq)
118     Result('high-smooth-freq%d'%i,
               locfreqplot('%s Local Frequency Smoothed %d'%(titlehigh,i)))
120
        # frequency residual
122     Flow('freqdif-filt%d'%i,'low-freq high-smooth-freq%d'%i,freqdif)
        Result('freqdif-filt%d'%i,freqdifplot(str(i)))
```

Listing 3: chapter-locfreq/merge/radius.c

```
/* smoothing radius (min = 1) */
2 #include <rsf.h>
#include <math.h>
4
int main (int argc, char* argv[])
6 {
    int n1, n1f, n2, n2f, i, n12, n12f;
8   float *rect, *fr, maxrad, c, *rad;
    sf_file in, out, freq;
10
    sf_init (argc,argv);
12
    in = sf_input("in");
14  freq = sf_input("freq");
    out = sf_output("out");
16
    if (!sf_histint(in,"n1",&n1)) sf_error("No n1= in input.");
18  if (!sf_histint(freq,"n1",&n1f)) sf_error("No n1= in frequency difference.");

20  n2 = sf_leftsize(in,1);
    n2f = sf_leftsize(freq,1);
22
    n12 = n1*n2;
24  n12f = n1f*n2f;

26  if (n1 != n1f) sf_error("Need matching n1");
    if (n2 != n2f) sf_error("Need matching n2");
28
    if (!sf_getfloat("c",&c)) c=1.;
30  if (!sf_getfloat("maxrad",&maxrad)) maxrad=1000.;

32  rect = sf_floatalloc(n12);
    sf_floatread(rect,n12,in);
34
    fr = sf_floatalloc(n12f);
36  sf_floatread(fr,n12,freq);
```

```
    rad = sf_floatalloc(n12);

    for (i=0; i < n12; i++) {

        /* update radius */
      rad[i] = rect[i]+c*fr[i];

        /* set constraint conditions: [1, maxrad] */
        if (rad[i] > maxrad)
                rad[i] = maxrad;
        if (rad[i] < 1.0)
                rad[i] = 1.0;
    }

    sf_floatwrite(rad,n12,out);
    exit(0);
}
```

Bibliography

Al-Inaizi, S., R. Bridle, and N. Nakhla, 2004, Comparison of pre and post-stack supermerge of ten 3D blocks: Presented at the 74th Annual International Meeting, SEG, Expanded Abstracts, Society of Exploration Geophysicists.

Aoki, N., and G. T. Schuster, 2009, Fast least-squares migration with a deblurring filter: GEOPHYSICS, **74**, WCA83–WCA93.

Bader, S., X. Wu, and S. Fomel, 2018, Missing log data interpolation and semiautomatic seismic well ties using data matching techniques: Interpretation. (Submitted).

Carter, D., and S. Pambayuning, 2009, Extended bandwidth by a frequency domain merge of two 3D seismic volumes: The Leading Edge, **28**, 386–386.

Casasanta, L., F. Perrone, G. Roberts, A. Ratcliffe, K. Purcell, A. Jafargandomi, and G. Poole, 2017, Applications of single-iteration Kirchhoff least-squares migration: Presented at the 87th Annual International Meeting, SEG, Expanded Abstracts, Society of Exploration Geophysicists.

Claerbout, J. F., 1992, Earth Soundings Analysis: Processing Versus Inversion: Blackwell Scientific Publications.

Dai, W., and G. T. Schuster, 2013, Plane-wave least-squares reverse-time migration: GEOPHYSICS, **78**, S165–S177.

Dong, S., J. Cai, M. Guo, S. Suh, Z. Zhang, B. Wang, and Z. Li, 2012, Least-squares reverse time migration: towards true amplitude imaging and improving the resolution: Presented at the 82nd Annual International Meeting, SEG, Expanded Abstracts, Society of Exploration Geophysicists.

Dutta, G., Y. Huang, W. Dai, X. Wang, and G. T. Schuster, 2014, Making the most out of the least (squares migration): 84th Annual International Meeting, SEG, Expanded Abstracts, 4405–4410.

Fomel, S., 2007a, Local seismic attributes: GEOPHYSICS, **72**, A29–A33.

———, 2007b, Shaping regularization in geophysical-estimation problems: GEOPHYSICS, **72**, R29–R36.

Fomel, S., M. Backus, K. Fouad, B. Hardage, and G. Winters, 2005, A multistep approach to multicomponent seismic image registration with application to a West Texas carbonate reservoir study: 75th Ann. Internat. Mtg, Soc. of Expl. Geophys., 1018–1021.

Fomel, S., and M. M. Backus, 2003a, Multicomponent seismic data registration by least squares: Presented at the 73rd Annual International Meeting, SEG, Expanded Abstracts, Society of Exploration Geophysicists.

———, 2003b, Multicomponent seismic data registration by least squares: 73rd Annual International Meeting, Soc. of Expl. Geophys., 701–784.

Fomel, S., and L. Jin, 2009, Time-lapse image registration using the local similarity attribute: GEOPHYSICS, **74**, A7–A11.

Fomel, S., P. Sava, I. Vlad, Y. Liu, and V. Bashkardin, 2013, Madagascar: open-source software project for multidimensional data analysis and reproducible computational experiments: Journal of Open Research Software, **1**, e8.

Gholamy, A., and V. Kreinovich, 2014, Why ricker wavelets are successful in processing seismic data: Towards a theoretical explanation: Presented at the 2014 IEEE Symposium on Computational Intelligence for Engineering Solutions (CIES), IEEE.

Greer, S., and S. Fomel, 2017a, Balancing local frequency content in seismic data using

non-stationary smoothing: 87th Annual International Meeting, SEG, Expanded Abstracts, Society of Exploration Geophysicists, 4278 – 4282.

———, 2017b, Matching and merging high-resolution and legacy seismic images: 87th Annual International Meeting, SEG, Expanded Abstracts, Society of Exploration Geophysicists, 5933 – 5937.

———, 2018, Matching and merging high-resolution and legacy seismic images: GEOPHYSICS, **83**, V115–V122.

Greer, S., Z. Xue, and S. Fomel, 2018, Improving migration resolution by approximating the least-squares hessian using non-stationary amplitude and frequency matching: Presented at the 88th Annual International Meeting, SEG, Expanded Abstracts, Society of Exploration Geophysicists.

Guitton, A., 2004, Amplitude and kinematic corrections of migrated images for nonunitary imaging operators: GEOPHYSICS, **69**, 1017–1024.

———, 2017, Fast 3D least-squares RTM by preconditioning with nonstationary matching filters: Presented at the 87th Annual International Meeting, SEG, Expanded Abstracts, Society of Exploration Geophysicists.

Hale, D., 2013, Dynamic warping of seismic images: GEOPHYSICS, **78**, S105–S115.

Hardage, B. A., M. V. DeAngelo, P. E. Murray, and D. Sava, 2011, Multicomponent seismic technology: Society of Exploration Geophysicists.

Herrera, R. H., S. Fomel, and M. van der Baan, 2014, Automatic approaches for seismic to well tying: Interpretation, **2**, SD9–SD17.

Herrera, R. H., and M. van der Baan, 2012, Guided seismic-to-well tying based on dynamic time warping: 82nd Annual International Meeting, Society of Exploration Geophysicists, 1–5.

Hestenes, M. R., and E. Stiefel, 1952, Methods of Conjugate Gradients for Solving

Linear Systems: Journal of Research of the National Bureau of Standards, **49**, 409–436.

Hou, J., and W. Symes, 2016, Accelerating least squares migration with weighted conjugate gradient iteration: Presented at the 78th EAGE Conference and Exhibition 2016, EAGE Publications BV.

Hou, J., and W. W. Symes, 2015, An approximate inverse to the extended born modeling operator: GEOPHYSICS, **80**, R331–R349.

Hu, J., and G. T. Schuster, 1998, Migration deconvolution: Presented at the Mathematical Methods in Geophysical Imaging V, SPIE.

Hu, J., G. T. Schuster, and P. A. Valasek, 2001, Poststack migration deconvolution: GEOPHYSICS, **66**, 939–952.

Kuehl, H., and M. D. Sacchi, 2003, Least-squares wave-equation migration for AVP/AVA inversion: GEOPHYSICS, **68**, 262–273.

Liu, Y., and S. Fomel, 2012, Seismic data analysis using local time-frequency decomposition: Geophysical Prospecting, **61**, 516–525.

Lumley, D., D. C. Adams, M. Meadows, S. Cole, and R. Wright, 2003, 4D seismic data processing issues and examples: 73rd Annual International Meeting, Society of Exploration Geophysicists, 1394–1397.

Meckel, T., N. L. Bangs, and T. Hess, 2017, 3D multichannel seismic field data from the San Luis Pass region off Galveston, Texas, acquired by the R/V Brooks-McCall in 2013 (BM1310).

Meckel, T. A., and F. J. Mulcahy, 2016, Use of novel high-resolution 3D marine seismic technology to evaluate Quaternary fluvial valley development and geologic controls on shallow gas distribution, inner shelf, Gulf of Mexico: Interpretation, **4**, SC35–SC49.

Mohan, T. R. M., C. B. Yadava, S. Kumar, K. K. Mishra, and K. Niyogi, 2007, Prestack merging of land 3D vintages — a case history from Kavery Basin, India: Presented at the 77th Annual International Meeting, SEG, Expanded Abstracts, Society of Exploration Geophysicists.

Müller, M., 2007, Dynamic time warping, *in* Information Retrieval for Music and Motion: Springer Berlin Heidelberg, 69–84.

Paffenholz, J., B. McLain, J. Zaske, and P. Keliher, 2002, Subsalt multiple attenuation and imaging: Observations from the Sigsbee2B synthetic dataset: 72nd Annual International Meeting, SEG, Expanded Abstracts, 2122–2125.

Petersen, C. J., S. Buenz, S. Hustoft, J. Mienert, and D. Klaeschen, 2010, High-resolution P-Cable 3D seismic imaging of gas chimney structures in gas hydrated sediments of an Arctic sediment drift: Marine and Petroleum Geology, **27**, 1981–1994.

Phillips, M., and S. Fomel, 2016, Seismic time-lapse image registration using amplitude-adjusted plane-wave destruction: 86th Annual International Meeting, SEG, Expanded Abstracts, Society of Exploration Geophysicists, 5473–5478.

Rickett, J. E., 2003, Illumination-based normalization for wave-equation depth migration: GEOPHYSICS, **68**, 1371–1379.

Ross, C. P., and M. S. Altan, 1997, Time-lapse seismic monitoring: Some shortcomings in nonuniform processing: The Leading Edge, **16**, 931–937.

Sacchi, M. D., J. Wang, and H. Kuehl, 2007, Estimation of the diagonal of the migration blurring kernel through a stochastic approximation: Presented at the 77th Annual International Meeting, SEG, Expanded Abstracts, Society of Exploration Geophysicists.

Schuster, G. T., 2017, Seismic inversion: Society of Exploration Geophysicists.

Tsinaslanidis, P., A. Alexandridis, A. Zapranis, and E. Livanis, 2014, Dynamic time warping as a similarity measure: Applications in finance: Presented at the Hellenic Finance and Accounting Association.

Ursenbach, C., P. Cary, and M. Perz, 2013, Limits on resolution enhancement for PS data mapped to PP time: The Leading Edge, **32**, 64–71.

White, R. E., 1991, Properties of instantaneous seismic attributes: The Leading Edge, **10**, 26–32.

Xue, Z., Y. Chen, S. Fomel, and J. Sun, 2016, Seismic imaging of incomplete data and simultaneous-source data using least-squares reverse-time migration with shaping regularization: GEOPHYSICS, **81**, no. 1, S11–S20.

Yu, J., J. Hu, G. T. Schuster, and R. Estill, 2006, Prestack migration deconvolution: GEOPHYSICS, **71**, S53–S62.

Zhou, J., J. Sun, and X. Ma, 2014, Application of Gabor transform to amplitude spectrum matching for merging seismic surveys: Presented at the 84th Annual International Meeting, SEG, Expanded Abstracts, Society of Exploration Geophysicists.

Vita

Sarah graduated with high honors from Cinco Ranch High School in Katy, Texas in 2014 and came to The University of Texas at Austin to pursue her undergraduate studies. She is a candidate for a Bachelor of Science degree in Geophysics from the Jackson School of Geosciences and a Bachelor of Science degree in Mathematics from the College of Natural Sciences. After graduation, she plans on pursuing a PhD in Mathematics and Computational Science at the Massachusetts Institute of Technology.

Permanent address: 2175 Stonecrest Drive, Eugene, OR, 97401, USA

This thesis was typeset with LaTeX[†] by the author.

[†]LaTeX is a document preparation system developed by Leslie Lamport as a special version of Donald Knuth's TeX Program.